

Disclosing Submillimeter Galaxy Formation: Mergers or Secular Evolution?

SIU-WANG CHAN(陳瀟弘) ^{1,2} YIPING Ao ^{1,2} AND QINGHUA TAN ^{1,2}

¹Purple Mountain Observatory, Chinese Academy of Science, 10 Yuanhua Road, Nanjing 210023, People's Republic of China

²School of Astronomy and Space Sciences, University of Science and Technology of China, Hefei 230026, People's Republic of China

ABSTRACT

We analyze the morphology of 125 submillimeter galaxies (SMGs) in the PRIMER-COSMOS field using double Sérsic modeling on JWST NIRC*am* images across six bands (F150W, F200W, F277W, F356W, F410M and F444W), with SMGs being classified by bulge Sérsic index (n_{bulge}) and bulge-to-total luminosity ratio (B/T). The Kolmogorov–Smirnov test between the bright ($SFR > 175 M_{\odot} yr^{-1}$) and the faint group ($SFR < 175 M_{\odot} yr^{-1}$) reveals no significant statistical differences in morphology across bands. However, we notice that SMGs skew towards higher B/T ratios and lower n_{bulge} from shorter to longer wavelengths. In F444W, bright SMGs exhibit higher B/T and lower n_{bulge} , indicating flatter, disturbed bulges, while faint SMGs show lower B/T and higher n_{bulge} . Notably, SMGs with higher B/T tend to have low Sérsic, challenging the local universe dichotomy of classical bulges ($B/T > 0.5$, $n > 4$) versus pseudo-bulges ($B/T < 0.35$, $n < 2$). In the F277W, non-parametric measurements indicate predominantly disk-dominated patterns, with only 24% of SMGs demonstrating merger signatures. After the removal of SMGs with disturbed morphology, the bulge classification scheme in F277W shows pseudo-bulges(21%) and clump migration bulges(16%) from secular evolution, compared to 4% merger-built bulges. Surprisingly, 48% of SMGs defy the classification scheme, showing high B/T (~ 0.7) but low Sérsic index ($n_{bulge} \leq 1$). Bars are confirmed in 7% of SMGs. This work suggests that secular evolution takes precedence over major mergers, supporting the idea that isolated evolution fueled by filamentary gas inflow plays a non-negligible role in the SMG bulge formation.

Keywords: (734) — Ultraluminous infrared galaxies (1735) — Galaxy structure (622) — Galaxy interactions (600) — Galaxy formation (595) — Galaxy mergers (608) — Galaxy bulges (578) — Infrared astronomy (786) — Submillimeter astronomy (1647)

1. INTRODUCTION

It is well known in the field that sub-millimeter galaxies play one of the most important roles at "cosmic noon" ($z \sim 2 - 3$), due to the fact that these systems harbor half of the star formation activities occurring over cosmic time, which are enshrouded by heavy dust (J. L. Puget et al. 1996; M. G. Hauser et al. 1998; U. Dudzevičiūtė et al. 2020). The dusty systems with high star formation rate ($SFR \sim 10^{2-3} M_{\odot} yr^{-1}$) systems, with extreme luminosity at far-IR and sub-mm wavelength ($L_{IR} \sim 10^{12-13} L_{\odot}$), containing a gas reservoirs of $M_{gas} \sim 10^{10-11} M_{\odot}$ (A. W. Blain et al. 2002; L. J. Tacconi et al. 2006; D. A. Riechers et al. 2010), are first uncovered by the Submillimeter Common-

User Bolometer Array(SCUBA) at 850 μm on the James Clark Maxwell Telescope(JCMT) in the late 1990s (I. Smail et al. 1997; D. H. Hughes et al. 1998; A. J. Barger et al. 1998), revolutionizing the way of studying extragalactic astronomy.

Numerous follow-up studies have been carried out across multiple bands, spanning optical to radio, to paint a full picture of these mysterious high- z galaxies throughout the decades. The heavy dust permeating among the plane of galactic disks causes the invisibility of SMGs at rest-frame UV/optical band, in the operation by either the space- and/or ground-based facilities, complicating the morphological confirmation (E. da Cunha et al. 2015), which results in several different naming variations for this type of galaxies, for example the "Dusty star forming galaxies(DSFGs)", "HST-

faint” , and ”NIR-Dark”(S. C. Chapman et al. 2004; J. M. Simpson et al. 2014; I. Smail et al. 2021) etc.

Due to its intense star formation activities and high infrared luminosity , it is natural for people to associate SMGs to ultraluminous infrared galaxies(ULIRGs) in the local universe(D. B. Sanders & I. F. Mirabel 1996; C. J. Lonsdale et al. 2006), suspecting similar formation patterns for these high- z systems. The majority of the ULIRGs($\sim 90\%$) are mostly assembled by major mergers , in which extreme starbursts are caused by gas compression , while for the SMGs , although previous studies using the Advanced Camera for Surveys (ACS) and Wide Field Camera 3 (WFC3) on the Hubble Space Telescope(HST) indicate 50 – 60% of merger rate(J. S. Kartaltepe et al. 2012; C.-C. Chen et al. 2015; C. J. Conselice et al. 2003; I. Smail et al. 2004) , recent high-resolution images from the JWST show only $\sim 20\%$ of the SMGs exhibiting tidal features(S. Gillman et al. 2024, 2023) , perplexing previous oversimplifications of their evolutionary pathways.

One of the most characteristic and complicated part of the SMGs is the dust-surrounded starburst core lied in the center of the galaxy , detected by the James Clark Maxwell Telescope(JCMT), the South Pole Telescope(SPT) , and the Atacama Large Millimeter/submillimeter Array(ALMA)(J. A. Hodge et al. 2016; B. Gullberg et al. 2019) , which plays an essential part in disclosing the formation truth and has yet to be fully understood. Several conjunctures have been brought up to account for the dilemma of formation mechanism: 1) major mergers driven , 2) violent disk instabilities , causing the clumps to migrate to the center , 3) cold gas accretion from the galaxy filaments(secular evolution). The major-merger origin (galaxy to galaxy mass ratio $\geq 1 : 4$) , is supported by the HST merger rate while being opposed by the merger rate derived based on the JWST data , possibly due to the interference of heavy dust extinction in previous studies(J. S. Kartaltepe et al. 2012; C.-C. Chen et al. 2015; A. M. Swinbank et al. 2010). Whereas the minor mergers , can indeed sustain graduate star formation, but yet being questioned for limited dynamical impact(J. A. Hodge et al. 2019; D. Narayanan et al. 2015). As for gas accretion , it serves as a good explanation for the disk-dominated morphology at high- z , but still struggles to explain the ultra-luminous SMGs(C. C. Hayward et al. 2013). None of these three monopolies on evolution mechanisms can fully account for the actual situation , suggesting a co-existence varying with luminosities and environments(C. M. Baugh et al. 2005; R. Davé et al. 2010; C. M. Casey et al. 2014).

In this work , we analyze the morphological properties of 125 statistically robust ALMA-detected SMGs in PRIMER-COSMOS field from Public Release IMaging for Extragalactic Research(PRIMER, Program ID:1837, PI: James S. Dunlop) , via two-dimensional decomposition and non-parametric analysis, as long as bar identification. The observational data are all presented here as part of the DAWN JWST Archive(DJA)(F. Valentino et al. 2023) , which includes fully reduced and pre-processed data using *grizli* pipeline(G. Brammer 2023) for all HST and JWST imaging data.

The structure of this paper is outlined below. Section 2 details the galaxy sample along with the photometric data. In Section 3 , we explain our methods for determining the galaxy morphology , including two-dimensional decomposition , merger identification , and bar identification strategies. Section 4 illustrates the results of our analysis , and further discussions are provided in Section 5. Throughout this paper , we assume that the Planck cosmology: $H_0 = 70.0 \text{ km.s}^{-1}$, $\Omega_M = 0.3$, $\Omega_\lambda = 0.7$.

2. DATA & SAMPLE SELECTION

To construct a sample of ALMA-detected galaxies with robust multi-wavelength coverage , we utilize the *A³COSMOS* (D. Liu et al. 2019; S. Adscheid et al. 2024) robust galaxy catalog³ as our parent catalog. The *A³COSMOS* project leverages archival ALMA (Atacama Large Millimeter/submillimeter Array) observations to study galaxy evolution , and the included catalog contains galaxies with secure ALMA detections (peak $S/N > 5.4$, lowest $S/N > 3$), with optical/near-infrared counterparts , and derived physical properties like stellar mass , redshift , and star formation rate(SFRs) etc. The *A³COSMOS* catalog incorporates 1.25 mm observations from 173 individual ALMA projects across 3233 pointings in the COSMOS field.

We then cross-match the ALMA positions for the SMGs with the photometric catalogs provided by the Dawn JWST Archive(DJA)(F. Valentino et al. 2023) of The Public Release IMaging for Extragalactic Research (PRIMER; Dunlop et al. 2021) survey. As a multi-wavelength , multi-instrument survey of UDS and COSMOS covering 234 and 144 arcmin² respectively , this extensive dataset provides deep NIRC*am* imaging. The observation consists of the seven wide-band and one medium-band NIRC*am* filter(F090W, F115Wt, F150W, F200W, F277W, F356W, F410M, F444W) , along with two wide-band MIRI filters(F770W, F1800W). Additionally, a portion of the PRIMER-COSMOS field is

³ <https://uni-bonn.sciebo.de/s/0LrfuA14s2YP3cz>

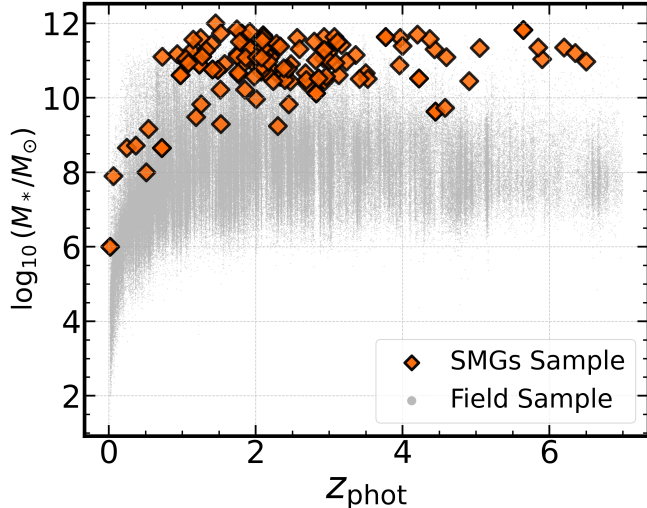


Figure 1. Photometric Redshift vs Stellar Mass for 125 selected SMGs(orange) , and the field sample(gray) in PRIMER-COSMOS field

covered by HST ACS and WFC3 coverage from CANDELS(N. A. Grogin et al. 2011), providing optical-to-near-infrared data ranging from $0.4\mu m$ to $1.6\mu m$. We excluded filters suffering from the issues of invisibility of the near-infrared counterparts (F090W, F115W) , and those with insufficient resolution for further analysis(F770W, F1800W) , which results in the remaining six bands(F150W, F200W, F277W, F356W, F410M, F444W) with robust detections of the JWST. Since detections in different wavelength, we convert the flux detected in different bands to $870\mu m$ via $f_{870\mu m}/f_{obs} = (\nu_{870\mu m}/\nu_{obs})^3$.

In the end , we obtained 125 unique sources detected by ALMA, with the complete catalog 6 in the Appendix. The median of $\log_{10}(M_*/M_\odot)$ is $10.98^{+0.53}_{-0.58}$ (16th to 84th percentile) , and the median redshift for our sample is $2.29^{+3.89}_{-1.48}$ (16th to 84th percentile) , which is consistent with the typical redshift range of the SMGs but skews toward higher redshift, dominating fainter end of the SMGs population($S_{870\mu m} = 1.88^{+1.28}_{-0.72} mJy$). The physical properties presented in this paper are all retrieved from the *A³COSMOS* project (S. Adscheid et al. 2024), in which they performed SED fitting with MAGPHYS, integrating ALMA sub-mm data with extensive ancillary data , including radio (e.g., VLA 1.4 GHz and 3 GHz), far-infrared (e.g., Herschel, Spitzer/MIPS 24 μm), and optical-to-near-infrared photometry. The uncertainties of the photometric redshift conform to $0.06(1+z)$, which is suitable for statistical measurements but not clusters proximity survey. As for stellar mass , the A3COSMOS paper excludes outliers and unreliable associations , ensuring a robust catalog with a

minimized chi-square error. The distribution of the redshift versus the stellar mass is shown in Figure 1. The median SFR is $185 M_\odot yr^{-1}$, with a 16th to 84th percentile ranging from $55 - 795 M_\odot yr^{-1}$.

3. METHODOLOGIES

In this section , we exhibit our methods to detail the morphological information of SMGs , including initial data reduction , two-dimensional(2D) parametric decomposition modeling , non-parametric approaches , along with bar identification techniques.

3.1. Data reduction

Firstly , we use the preprocessed *JWST* data provided by the Dawn *JWST* Archive (DJA). The data reduction pipeline , as detailed in (F. Valentino et al. 2023), processes level-2 NIRCcam products with GRIZLI , applying zero-point corrections and artifact removal, then aligns them with the HST Complete Hubble Archive for Galaxy Evolution (V. Kokorev et al. 2022) data to Gaia DR3(Gaia Collaboration et al. 2021) at $0''.02 - 0''.04$ pixel scales. By checking the quality of the image obtained from the DJA , we ensure that they are eligible for further morphological studies , with *flag* = 2. Then , we make $6.5'' \times 6.5''$ image cutouts for each source , based upon the background-subtracted images provided by the DJA , which are centered on their respective NIRCcam detection coordinates. By using PHOTUTILS (L. Bradley et al. 2024) , we mask the surrounding area to suppress interference, keeping values higher than the 2σ threshold in the exact center of the source. We perform this procedure on all of these six *JWST* NIRCcam bands (F150W, F200W, F277W, F356W, F410M, F444W). Both parametric and nonparametric morphological analyses are performed on these cutouts. As for the Point Spread Function(PSF) , we use the ones provided by the DJA , which are generated using PSFex(E. Bertin 2013) based on the custom selection methods MU_MAX/MAG_AUTO plane(A. Leauthaud et al. 2007) to yield better results than the default auto-selection from PSFEx.

3.2. Parametric Morphology

For parametric analysis , we focus primarily on the double Sérsic fitting , exploring the origins of the SMGs population by leveraging the properties of the bulge , specifically the bulge Sérsic index and the bulge-to-total luminosity ratio (B/T). The assumption of distinctions between the two evolution pathways is presented in Figure 2. We perform single- and double-component light profile fittings on our sample. Using the results of the single profile fitting as reference of the double sersic fitting and those of the previous studies , we set up the

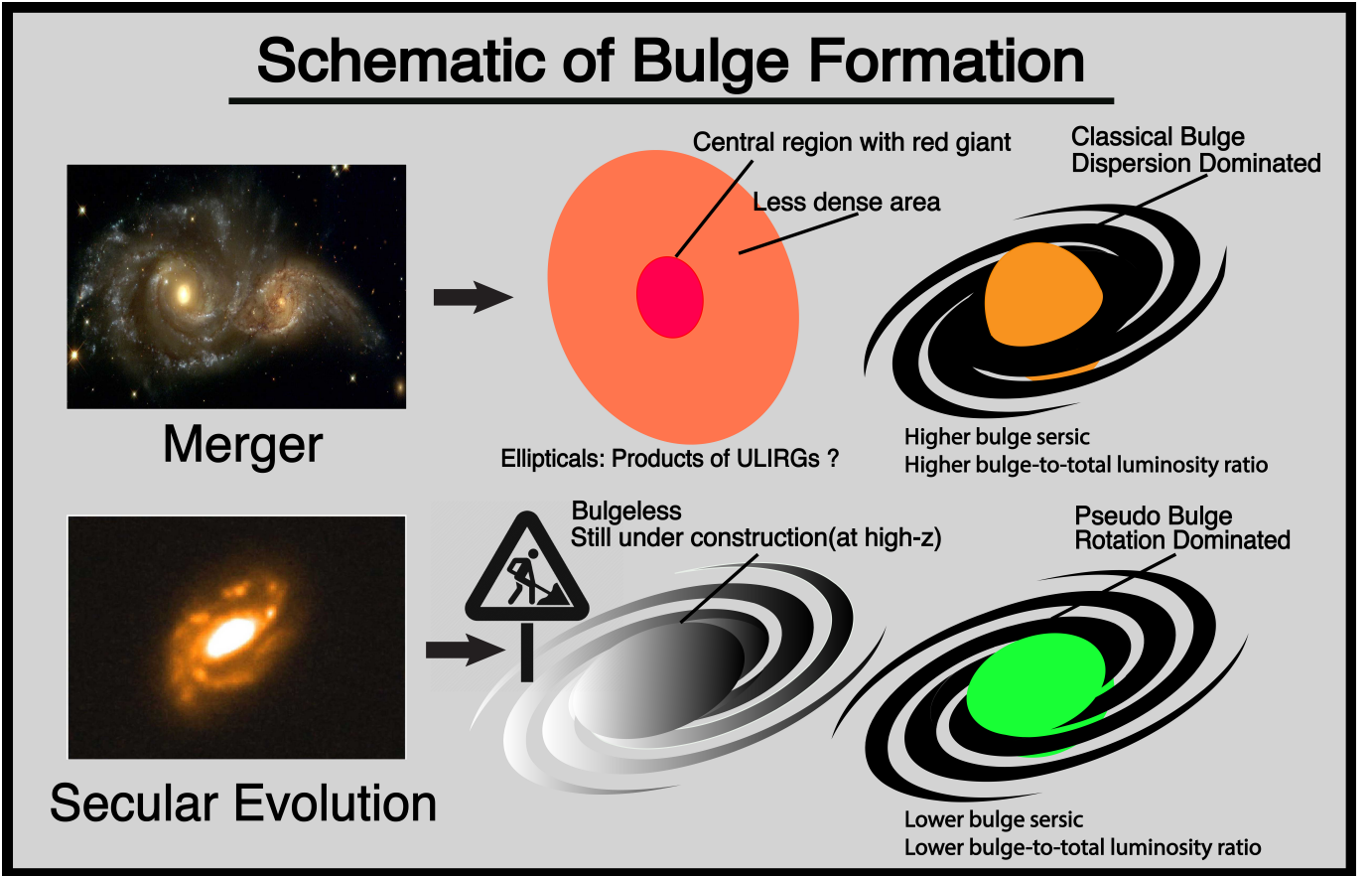


Figure 2. Simple assumptive sketch based on previous studies summarizing the bulge formations in submillimeter galaxies presented in this paper , in which the classical bulge and ellipticals(kinematically hot, high B/T , high Sérsic) are the products of mergers whereas the pseudobulges and the bulgeless galaxies(kinematically cold, low B/T , low Sérsic) are fabricated by degrees in the secular evolution.

priors for the double profile fitting on this basis , to improve the accuracy and credibility of the results.

3.2.1. Single Sérsic fitting

We implemented our parametric modelings on the optical and near-infrared counterparts using **PySersic** (I. Pasha & T. B. Miller 2023) , a Python-based code using Bayesian inference to fit the Sérsic profile to the galaxy light distributions. **PySersic** is built on JAX (J. Bradbury et al. 2018) for efficient numerical computation and utilizes NUMPYRO (D. Phan et al. 2019) for probabilistic inference. Compared to traditional methods such as **Galfit**(C. Y. Peng et al. 2010) , which rely on least squares fitting , **PySersic** performs parameter estimations by sampling the posterior distributions , using the No U-Turn Sampler(NUTS) methods. There is no significant systematic difference between the results obtained by the two , which has been tested in recent studies on post-starburst galaxies(Y. Zhang et al. 2024) and on SMGs (J. Ren et al. 2025a).

We examine our results by comparing them with recent work on SMGs(J. Ren et al. 2025a), including the

sersic index and the physical size. The results of the single Sérsic modeling show overall good consistency , and details are shown in Figure 10 in the Appendix.

3.2.2. Double Sérsic fitting

In order to derive morphological information based on the bulges of the SMGs in more detail , we then perform the double Sérsic profiles on our samples , with the double Sérsic profile and a flat sky background fitted simultaneously.

The Sérsic model profile fitted to both bulges and discs is:

$$I(R) = I_e \exp\left\{-b_n \left[\left(\frac{R}{R_e}\right)^{1/n} - 1\right]\right\} \quad (1)$$

where R is the radius to the center of the galaxy , R_e (effective radius) serves as the radius that contains half of the total light/mass , I_e is the intensity at that radius , b_n is a constant solely dependent on n (I. Trujillo et al. 2004) , and n measures the concentration of the overall light profile. When $n=1$, the Sérsic profile reduces to an exponential profile that describes a pure

disk , while $n=4$ corresponds to the de Vaucouleurs profile that describes an elliptical galaxy.

To ensure credible results of the double Sérsic fitting , we manually set the prior for the effective radius of both the bulge and the disc , as well as the Sérsic index n_bulge of the bulge. The effective radius for the bulge , Re_bulge , follows a truncated Gaussian centered at 1 kpc , with a 50 % standard deviation and bounds from 0 to 2 kpc , while Re_disk (the effective radius for the disc component) was centered at 4 kpc , with a truncated boundary from 2 to 12 kpc. The Sérsic n_bulge was assigned a loose Gaussian prior centered at 2.0 (standard deviation = 1.0) to favor a bulge-like structure , while n_disk (Sérsic index of the disc) and the prior of all the remaining parameters are estimated by the *autoprior()* function, ensuring flexibility for disc-like components and robust fits across our galaxy sample. We then sequentially fit each band: F150W, F200W, F277W, F356W, F410M, and F444W.

In the end , we obtain several parameters via Sérsic modeling through *PySersic*: the total integrated flux $flux$, the position of Sérsic modeling (x_c , y_c), the fraction of luminosity contained in the inner component (namely the bulge to total ratio) f_1 , the position angle θ , the ellipticity of both the bulge e_1 and the disc e_2 , the effective radius of both the bulge r_1 and disk r_2 , the Sérsic index of bulge n_bulge and disc n_disk . Due to various factors (such as low-quality imaging , contamination from neighboring sources , and incomplete data) , the total number of galaxies found in each band may decrease compared to the original sample.

3.3. Non-Parametric Morphology

In order to obtain more robust and comprehensive indicators , we then apply the nonparametric analysis to these samples using the *statmorph* (V. Rodriguez-Gomez et al. 2019) package. The package focuses on the derivations of the CAS system (C. J. Conselice 2003) , $Gini$ & M_{20} (J. M. Lotz et al. 2004) , and other important morphological indicators. By checking the signal-to-noise ratio (SNR) for each aperture in the provided DJA catalogue , we confirm that the vast majority of the SMGs in our sample are eligible for the non-parametric measurement ($SNR \leq 3$) , with only ≤ 3 SMGs with $SNR \leq 3$. We then run this routine on both SMGs and field samples on band F277W because of the completeness of the image data compared to other bands , with the majority of them having a "good" fit results ($Flag = 0$). Several factors can be cited to explain the reason with results that are of poor quality ($Flag \neq 0$) , for example , artifacts , sources that are too faint and dis-

torted , and the crowd environment causes the inefficiency of masking the surrounding sources.

3.3.1. CAS System

The CAS system is widely used in many classification scenarios. The C in the CAS system stands for the concentration index , which is defined as:

$$C = 5 \log \frac{R_{80}}{R_{20}}$$

where R_{20} and R_{80} represent the radius that contains 20 percent and 80 percent of the total luminosity , respectively.

A , the asymmetry index , is calculated by subtracting the galaxy image by rotating 180° from the original one; the exact mathematical expression can be written as:

$$A = \frac{\sum_{i,j} |f_{i,j} - f_{i,j}^{180^\circ}|}{\sum_{i,j} |f_{i,j}|} - A_{bkg}$$

with $f_{i,j}$ and $f_{i,j}^{180^\circ}$ represents the flux of each individual pixel of the image and the one after rotating the image by 180° , respectively. A_{bkg} is the average background asymmetry.

The Smoothness (or Clumpiness) index , S , describes the smoothness of the galaxy light distribution. It is obtained by subtracting the original galaxy image with the smooth version of it which has already been convolved with a Gaussian kernel to smooth out the details with high spatial frequency and preserve the one with low spatial frequency. By applying this procedure , structures with high spatial frequency can be emphasized for further analysis. The equation has a similar form with the one above:

$$S = \frac{\sum_{i,j} |f_{i,j} - f_{i,j}^s|}{\sum_{i,j} |f_{i,j}|} - S_{bkg}$$

where $f_{i,j}$ and $f_{i,j}^{180^\circ}$ represent the flux of each individual pixel of the image and the one after rotating the image by 180° , respectively. S_{bkg} is the smoothness of the background.

3.3.2. Gini- M_{20} Diagram

One of the most commonly used merger classification methods is the $Gini - M_{20}$ diagram , which is used to select the one with potential merger activity from those non-mergers. To explain it concisely , the Gini coefficient was first introduced in the economics field to describe the inhomogeneous distribution of wealth across different classes. In galactic morphology , it measures the relative distribution of flux over pixels assigned to the particular galaxy , with $Gini = 1$ corresponds to

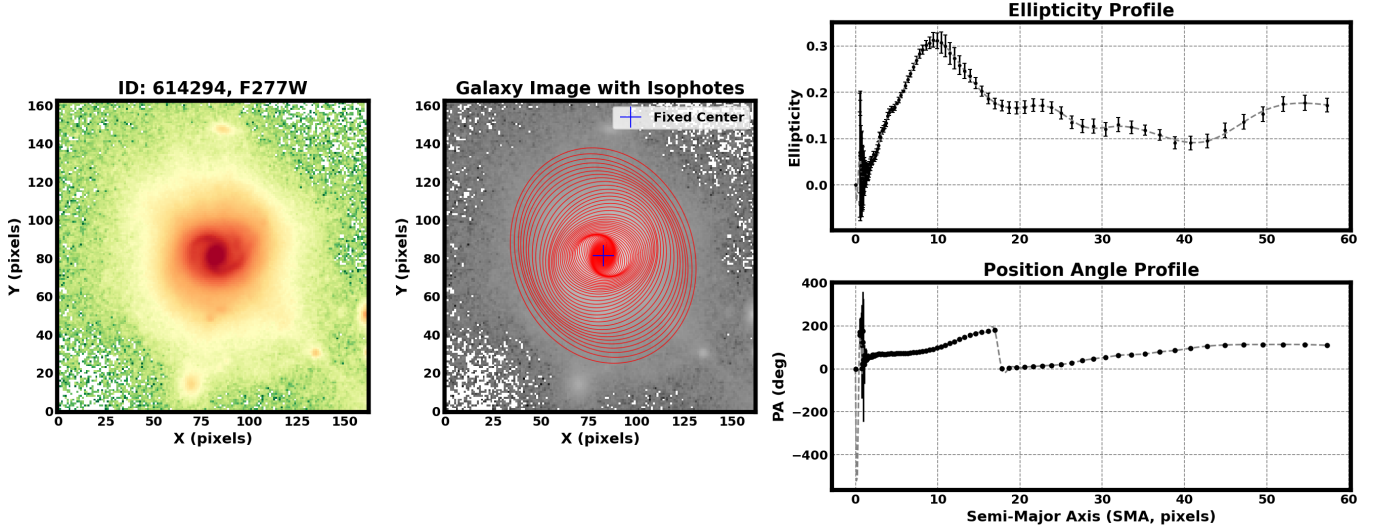


Figure 3. An example of bar identification via ellipse isophotal fitting of source ID: 614294 via ellipse-fitting techniques as an example. The blue cross marks the shared center of isophotes (red).

all of the light concentrated on one single pixel, while light spreads evenly across all pixels when $Gini = 0$. The Gini coefficient of a galaxy with n pixels can be calculated by the following equation:

$$G = \frac{1}{\bar{f}n(n-1)} \sum_{i=1}^n (2i - n - 1) f_i$$

where f_i is the flux of the i th pixel, and \bar{f} is the mean of the flux value.

The M_{20} provides information regarding the normalized second-order moment of the brightest 20 percent of the galaxy's pixel, which is normalized by the total moment for all pixels. Galaxies with brighter, clumpy fragments have a larger value, whereas those with fewer fragments and a less dispersed light distribution have lower values. For galaxies with n pixel, the M_{20} can be calculated by the following expression:

$$M_{tot} = \sum_i^n M_i = \sum_i^n f_i [(x_i - x_c)^2 + (y_i - y_c)^2]$$

in which f_i stands for the flux measured at i th pixel, and the (x_c, y_c) is the central position that minimize the M_{20} .

3.4. Bar identification

There are numerous approaches to identify a stellar bar within galaxies (P. B. Nair & R. G. Abraham 2010; M. Herrera-Endoqui et al. 2015; G. de Vaucouleurs et al. 1991; K. Menéndez-Delmestre et al. 2007; I. Marinova & S. Jogee 2007; K. Sheth et al. 2008; S.-Y. Yu & L. C. Ho 2020; D. A. Gadotti 2009; E. Laurikainen et al. 2005;

H. Salo et al. 2015), including visual inspection, two-dimensional decomposition, Fourier analysis, and ellipse isophotal fitting techniques. Each has its own costs and benefits. Several studies have been carried out to pinpoint the stellar bar within the high- z galaxies leveraging ellipse fitting since the advent of the JWST (X. Liang et al. 2024; Z. A. Le Conte et al. 2024; Y. Guo et al. 2023). Taking all of the factors into account, we refer to the methods used in the previous research and follow them after tailored to our dataset. We employ three-step bar identification procedures, combining visual inspection, ellipse-fitting, and Sérsic fitting residuals.

1. **Visual Inspection:** We visually check the cutouts to remove the one with high inclination and the one being too faint to be detected or contaminated by nearby sources, in which we perform an initial search for the candidates for stellar bar.
2. **Ellipse Isophotal Fitting:** We used the photutils.isophote Ellipse package to identify the stellar bar in galaxy images via two-stage isophotal fitting process. We fit isophotes with free center (x_0, y_0), ellipticity (ϵ), and the position angle (PA), using an initial SMA of 5 pixels, $\epsilon = 0.2$, $PA = 0$, $step_size = 0.1$, and $max_SMA = 30$ pixels, with median integration and 3-sigma clippings. The galaxy center was set as the mean of the inner isophote centers. We then fix the center and fit isophotes up to $SMA = 60$ pixels with a step-size of 0.05, ensuring the center stability ($< 10^{-6}$ pixel variation). We identified bar candidates by detecting the $\epsilon (> 0.1)$ peaks in the profile, and visually

compared them against bar-like features by comparing raw and isophote-overlaid images. An example using the ellipse isophote fitting method is shown in Fig. 3.

3. **Sérsic Fitting Residuals:** Last but not least, we examined the residuals of single Sérsic fittings to ensure the reliability of the identification results, which highlights the elongated structures consistent with bars provided additional evidence, ensuring robust classification.

Bar candidates require either visual inspection or ellipse fitting confirmation to be labeled as 'tentative' but require both methods for confirmation. The final bar confirmation is determined by the presence of bar-like features in the Sérsic residuals. The residuals of the confirmed bar candidates via single Sérsic modellings are shown Fig 12 in the appendix.

4. RESULTS

4.1. Morphological parameters across bands

We measure the half-light radius and Sérsic indices (including bulges and discs) of SMGs across the six bands. We use the $r_{\text{hat}} \approx 1.0$ to assess the convergence of the Markov Chain Monte Carlo (MCMC) measurements, making sure that all markov chains are all converged to same underlying distribution of the results. The overall results of the properties is shown in Table 1, and an intuitive plot about the effective radii of the bulge and the disk is displayed in Fig 5. To make it concise, we show the median values of effective radius and Sérsic indices of band F150W and F444W, with median values of half-light radius $R_{\text{bulge}}^{F150W} = 1.18 \pm 0.41 \text{ kpc}$, $R_{\text{disc}}^{F150W} = 5.74 \pm 3.65 \text{ kpc}$, $R_{\text{bulge}}^{F444W} = 1.35 \pm 0.51 \text{ kpc}$, $R_{\text{disc}}^{F444W} = 4.19 \pm 3.58 \text{ kpc}$, and median values of Sérsic indices $n_{\text{bulge}}^{F150W} = 2.03 \pm 0.75$, $n_{\text{disc}}^{F150W} = 0.68 \pm 0.42$, $n_{\text{bulge}}^{F444W} = 0.98 \pm 1.52$, and $n_{\text{disc}}^{F444W} = 0.72 \pm 0.71$. The overall results of the physical size show values comparable with the optical size of the rest frame and the infrared size of the rest frame measured by S. J. McKay et al. (2025), J. Ren et al. (2025a), S. Gillman et al. (2024), and J. McKinney et al. (2025). Several factors can be considered when it comes to the offset between the results and the one from previous works. One of the most notable causes is that single Sérsic modeling considers the light distribution of the bulge and disc as a whole, making the half-light radius larger than the one from the bulge and slightly smaller than the one of the disc derived from double Sérsic modeling, which is also proved by one of the first JWST works (C.-C. Chen et al. 2022). Factors such as sample selection criterion

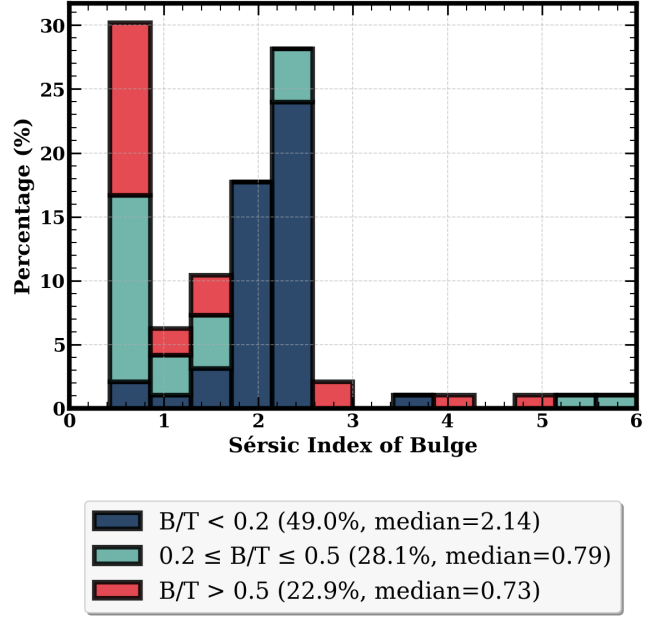


Figure 4. The distribution of bulge Sérsic indices across three B/T bins ($B/T < 0.2$, $0.2 \leq B/T \leq 0.5$, $B/T > 0.5$) in band F200W.

and approaches used to measure the light distribution can be taken into account to explain the discrepancy.

In addition to physical size and light distribution index, we also measure the bulge-to-total luminosity ratio (B/T), which presents the fraction of total luminosity contributed by the bulge component of the galaxy. For simplicity, we only show the median value of B/T of band F150W and F444W, with $B/T^{F150W} = 0.09 \pm 0.26$ and $B/T^{F444W} = 0.58 \pm 0.33$.

To ensure the credibility of our results, we perform the accuracy test on our results of single Sérsic and double Sérsic fitting in F277W. The overall results show that the accuracy of the single Sérsic shows $97.3\%^{+1.53}_{-6.46}$ for the n , and $98.4\%^{+1.0}_{-3.5}$ for the r_{eff} . The accuracy of the double Sérsic shows that $91.2\%^{+6.5}_{-60.1}$ for the f_{b} , $81.8\%^{+13.8}_{-9.5}$ for the n_{bulge} , $93.9\%^{+5.3}_{-15.2}$ for n_{disc} , $87.2\%^{+11.0}_{-14.1}$ for Re_{bulge} , $92.3\%^{+5.8}_{-11.4}$ for Re_{disc} .

4.1.1. SFR dependent Morphology

To establish the idea whether the bright and faint population of SMGs is subjected to the same distribution, we divide our samples into two bins: one with $\text{SFR} < 175 M_{\odot} \text{ yr}^{-1}$, and the other with $\text{SFR} > 175 M_{\odot} \text{ yr}^{-1}$. We then performed the Kolmogorov-Smirnov (KS) test on the frequency distribution of B/T and Sérsic index of the bulge between these two groups. Table 2 summarizes results for all bands.

In general, there are no significant statistical differences across the board. In particular, we highlight the F444W due to its longest wavelength, which enables

Band (N)	Re_bulge [kpc]	Re_disk [kpc]	n_bulge	n_disk	B/T
F150W (N=116)	$1.18^{+0.26}_{-0.11}$	$5.43^{+4.93}_{-1.85}$	$2.00^{+1.04}_{-1.04}$	$0.69^{+0.44}_{-0.44}$	$0.09^{+0.26}_{-0.26}$
F200W (N=100)	$1.19^{+0.51}_{-0.11}$	$4.36^{+3.35}_{-1.15}$	$1.90^{+1.09}_{-1.09}$	$0.69^{+0.73}_{-0.73}$	$0.22^{+0.31}_{-0.31}$
F277W (N=125)	$1.45^{+0.51}_{-0.38}$	$3.99^{+2.78}_{-0.89}$	$1.47^{+1.85}_{-1.85}$	$0.71^{+1.00}_{-1.00}$	$0.46^{+0.31}_{-0.31}$
F356W (N=106)	$1.42^{+0.60}_{-0.32}$	$4.10^{+2.73}_{-1.30}$	$1.33^{+1.81}_{-1.81}$	$0.71^{+0.97}_{-0.97}$	$0.53^{+0.31}_{-0.31}$
F410M (N=99)	$1.29^{+0.60}_{-0.22}$	$4.23^{+2.88}_{-1.45}$	$1.63^{+1.47}_{-1.47}$	$0.71^{+0.93}_{-0.93}$	$0.47^{+0.34}_{-0.34}$
F444W (N=99)	$1.26^{+0.69}_{-0.20}$	$4.19^{+2.58}_{-1.41}$	$1.48^{+1.51}_{-1.51}$	$0.72^{+0.67}_{-0.67}$	$0.58^{+0.33}_{-0.33}$

Table 1. Summary of physical properties of SMGs across six JWST bands. The columns represent the effective radii of the bulge and disk ($r_{\text{eff},1}$ and $r_{\text{eff},2}$), their Sérsic indices (n_bulge and n_disk), and the bulge-to-total luminosity ratio (B/T).

Band	Faint (%)	Bright (%)	B/T (F)	B/T (B)	$p\text{-val}$ (B/T)	n_{bulge} (F)	n_{bulge} (B)	$p\text{-val}$ (n_{bulge})
F150W	53.3%	46.7%	0.06 ± 0.03	0.10 ± 0.03	0.384	3.91 ± 0.17	3.83 ± 0.18	0.057
F200W	55.7%	44.3%	0.22 ± 0.04	0.28 ± 0.04	0.686	3.54 ± 0.19	3.08 ± 0.22	0.974
F277W	50.9%	49.1%	0.40 ± 0.03	0.39 ± 0.03	0.929	2.31 ± 0.22	2.38 ± 0.25	0.652
F356W	54.0%	46.0%	0.43 ± 0.03	0.45 ± 0.04	0.922	2.23 ± 0.21	2.06 ± 0.24	0.769
F410M	53.6%	46.4%	0.35 ± 0.03	0.42 ± 0.04	0.905	2.92 ± 0.18	2.72 ± 0.22	0.899
F444W	53.6%	46.4%	0.32 ± 0.03	0.37 ± 0.04	0.459	2.79 ± 0.22	2.30 ± 0.25	0.510

Table 2. KS test results for bulge-to-total ratio (B/T) and bulge Sérsic index (n_{bulge}) between faint (“F”, $\text{SFR} < 185 M_{\odot} \text{ yr}^{-1}$) and bright (“B”, $\text{SFR} \geq 185 M_{\odot} \text{ yr}^{-1}$) SMGs across JWST bands. Percentages (cols. 2–3) give the fraction of sources in each subgroup. Values reported are medians \pm uncertainty (as you supplied). The p -values are from two-sample Kolmogorov–Smirnov tests; we treat distributions as indistinguishable when $p > 0.05$.

Band	Bulge ($Re_bulge/$ kpc)			Disk ($Re_disk/$ kpc)		
	$\text{SFR} < 175 M_{\odot} \text{ yr}^{-1}$	$\text{SFR} \geq 175 M_{\odot} \text{ yr}^{-1}$	P-value	$\text{SFR} < 175 M_{\odot} \text{ yr}^{-1}$	$\text{SFR} \geq 175 M_{\odot} \text{ yr}^{-1}$	P-value
F150W	1.17 ± 0.05	1.11 ± 0.06	0.354	4.81 ± 0.40	6.28 ± 0.53	0.065
F200W	1.19 ± 0.06	1.14 ± 0.06	0.141	4.23 ± 0.38	5.05 ± 0.59	0.268
F277W	1.30 ± 0.06	1.50 ± 0.06	0.335	3.75 ± 0.29	4.43 ± 0.47	0.072
F356W	1.28 ± 0.07	1.47 ± 0.07	0.598	3.74 ± 0.35	4.96 ± 0.57	0.020
F410M	1.16 ± 0.06	1.34 ± 0.07	0.396	3.81 ± 0.37	4.61 ± 0.65	0.043
F444W	1.20 ± 0.07	1.35 ± 0.08	0.725	3.97 ± 0.36	4.62 ± 0.62	0.017

Table 3. Effective radii for bulges (Re_bulge) and disks (Re_disk) across six bands, split by SFR (in $M_{\odot} \text{ yr}^{-1}$). Bold p -values (< 0.05) show disks expand as the star formation rate rises.

better penetration through dust, providing a clearer view of the stellar structures within SMGs. In F444W, bright SMGs exhibit a B/T of 0.60 ± 0.05 and n_bulge of 0.91 ± 0.27 , while the faint ones show a B/T of 0.52 ± 0.04 and n_bulge of 1.58 ± 0.18 , with $p\text{-value} > 0.05$ showing no significant distinctions between these two groups. Although $p < 0.05$ in the F150W, we find no significant statistical difference between these two groups by checking the cdf diagram between the groups.

In addition, we perform the KS test on the effective radii of the bulge component and the disk component. The results are shown in Table 3, which shows larger radii in both the bulge and the disk of the bright pop-

ulation comparing it to the faint ones across the board. The $p\text{-values}$ in the F356W, F410M, and F444W show an even greater distinction between the two groups.

4.1.2. Structural trend by B/T

To explore the evolving structural trend of the bulges within the center of the SMGs, we group them into three B/T bins: $B/T < 0.2$, $0.2 < B/T < 0.5$, and $B/T > 0.5$, based upon previous splits by SFR. We discard the results with poor quality, by setting a mask to rule out the one with the negative flux (fitting results for each band). Detailed information on the B/T splits can be found in Table 4 (with a more intuitive plot of the distribution of bulge Sérsic indices divided by three

Band	B/T Bin	Faint ($SFR < 175 M_{\odot} \text{ yr}^{-1}$)		Bright ($SFR \geq 175 M_{\odot} \text{ yr}^{-1}$)	
		Fraction (%)	n_{bulge} (Median)	Fraction (%)	n_{bulge} (Median)
F150W	< 0.2	62.3% (43/69)	$2.03^{+0.15}_{-0.54}$	63.8% (30/47)	$2.19^{+0.03}_{-0.13}$
	$0.2-0.5$	21.7% (15/69)	$1.20^{+0.43}_{-0.46}$	23.4% (11/47)	$1.07^{+0.68}_{-0.40}$
	> 0.5	15.9% (11/69)	$1.25^{+0.45}_{-0.55}$	12.8% (6/47)	$1.06^{+0.12}_{-0.33}$
F200W	< 0.2	44.3% (27/61)	$2.13^{+0.05}_{-0.17}$	53.8% (21/39)	$2.19^{+0.05}_{-0.17}$
	$0.2-0.5$	29.5% (18/61)	$0.76^{+0.75}_{-0.09}$	28.2% (11/39)	$1.41^{+0.84}_{-0.72}$
	> 0.5	26.2% (16/61)	$0.73^{+0.70}_{-0.06}$	17.9% (7/39)	$0.75^{+0.30}_{-0.08}$
F277W	< 0.2	30.6% (22/72)	$2.15^{+0.13}_{-0.37}$	22.6% (12/53)	$2.22^{+0.05}_{-0.01}$
	$0.2-0.5$	27.8% (20/72)	$1.28^{+3.00}_{-0.58}$	28.3% (15/53)	$1.47^{+1.47}_{-0.80}$
	> 0.5	41.7% (30/72)	$0.75^{+1.14}_{-0.09}$	49.1% (26/53)	$0.76^{+1.71}_{-0.10}$
F356W	< 0.2	23.8% (15/63)	$2.23^{+1.12}_{-0.06}$	20.9% (9/43)	$2.21^{+1.55}_{-0.02}$
	$0.2-0.5$	19.0% (12/63)	$3.01^{+1.79}_{-2.02}$	25.6% (11/43)	$1.61^{+4.29}_{-0.94}$
	> 0.5	57.1% (36/63)	$0.72^{+1.20}_{-0.06}$	53.5% (23/43)	$0.69^{+0.33}_{-0.04}$
F410M	< 0.2	28.8% (17/59)	$2.20^{+0.10}_{-0.09}$	25.0% (10/40)	$2.25^{+0.24}_{-0.03}$
	$0.2-0.5$	20.3% (12/59)	$2.57^{+1.40}_{-1.79}$	30.0% (12/40)	$2.54^{+1.78}_{-1.84}$
	> 0.5	50.8% (30/59)	$0.68^{+0.61}_{-0.02}$	45.0% (18/40)	$0.70^{+0.35}_{-0.04}$
F444W	< 0.2	28.8% (17/59)	$2.21^{+1.00}_{-0.10}$	20.0% (8/40)	$2.24^{+1.14}_{-0.02}$
	$0.2-0.5$	18.6% (11/59)	$3.22^{+1.54}_{-0.84}$	15.0% (6/40)	$4.35^{+0.48}_{-1.22}$
	> 0.5	52.5% (31/59)	$0.67^{+0.85}_{-0.01}$	65.0% (26/40)	$0.68^{+0.24}_{-0.03}$

Table 4. Distribution of bulge Sérsic index n_{bulge} in B/T bins for faint ($SFR < 175 M_{\odot} \text{ yr}^{-1}$) and bright ($SFR \geq 175 M_{\odot} \text{ yr}^{-1}$) SMGs in different JWST bands. Fractions in each bin are shown along with the median n_{bulge} and asymmetric errors.

Bulge Type (N)	Stellar Mass ($10^{11} M_{\odot}$)	SFR ($M_{\odot} \text{ yr}^{-1}$)	B/T	Sérsic n	R_{eff} (kpc)
Classical Bulge (N=27)	$1.6^{+1.1}_{-0.9}$	$162.2^{+200.9}_{-73.1}$	$0.3^{+0.2}_{-0.1}$	$4.6^{+1.1}_{-1.9}$	$2.0^{+0.0}_{-0.5}$
Major Merger Bulge (N=4)	$1.3^{+1.3}_{-0.9}$	$152.5^{+273.6}_{-116.6}$	$0.6^{+0.1}_{-0.0}$	$4.4^{+1.0}_{-0.2}$	$1.4^{+0.7}_{-0.7}$
Clump Sinking Bulge (N=16)	$1.6^{+0.6}_{-0.4}$	$204.4^{+294.2}_{-95.5}$	$0.5^{+0.1}_{-0.1}$	$2.7^{+0.6}_{-0.3}$	$2.0^{+0.1}_{-0.6}$
Pseudo Bulge (N=21)	$0.8^{+0.4}_{-0.4}$	$151.4^{+137.1}_{-122.5}$	$0.1^{+0.1}_{-0.1}$	$1.4^{+0.8}_{-0.6}$	$1.1^{+0.6}_{-0.1}$
Unclassified Bulge (N=47)	$0.9^{+0.9}_{-0.6}$	$128.8^{+153.3}_{-52.0}$	$0.7^{+0.2}_{-0.2}$	$0.7^{+0.2}_{-0.0}$	$1.6^{+0.3}_{-0.3}$

Table 5. Median of the physical properties by bulge type, with the lower and upper bounds corresponding to the 25th and 75th percentiles. All values are rounded to one decimal place.

B/T bins in Appendix 9). Intriguingly, it turns out that there is an apparent trend within the distribution. SMGs with higher B/T bin lean towards lower bulge's lower Sérsic index, whilst the ones with lower B/T sit right at the position with higher Sérsic index (with an example in band F200W shown in Fig 4).

For the faint SMGs, the low B/T bin ($B/T < 0.2$) leads in shorter-wavelength bands, capturing 62.3% (43/69) in F150W and 44.3% (27/61) in F200W, with $n_{bulge} = 2.03-2.23$ ($\sigma = 0.36-1.30$). These high n_{bulge} values reflect steep, compact bulges. The intermediate bin ($0.2 < B/T < 0.5$, 18.6–29.5%) shows

transitional profiles with $n_{bulge} = 0.76-3.22$ ($\sigma = 1.58-2.31$), while the high B/T bin (15.9–57.1%) dominates in longer wavelengths, peaking at 57.1% (36/63) in F356W and 52.5% (31/59) in F444W, with $n_{bulge} = 0.67-1.25$ ($\sigma = 0.98-2.06$), indicating flatter profiles.

For the bright SMGs, the whole picture shifts slightly. The low B/T bin remains prominent in F150W (63.8%, 30/47) and F200W (53.8%, 21/39), with $n_{bulge} = 2.19-2.25$ ($\sigma = 0.32-0.76$), mirroring the faint SMGs' compact bulges. The intermediate bin (15.0–30.0%) yields $n_{bulge} = 1.07-4.35$ ($\sigma = 0.98-2.81$), but the high B/T bin surges in longer wavelengths, reaching

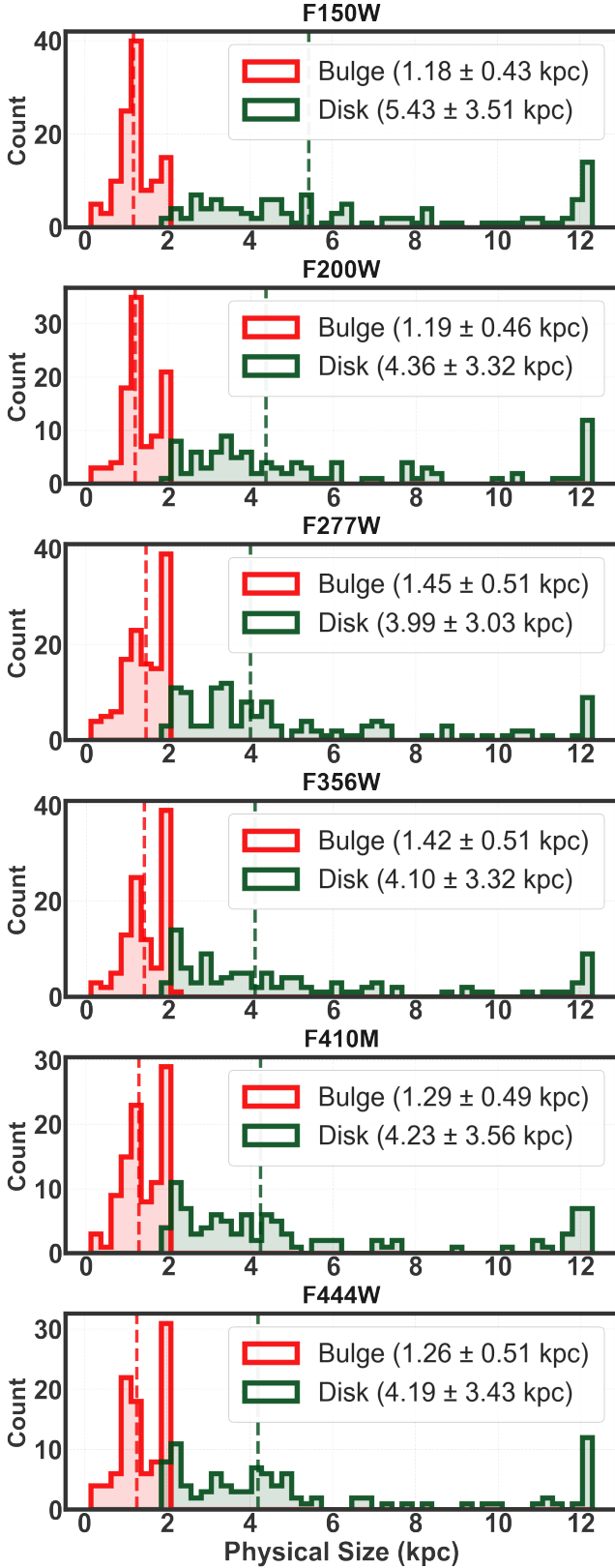


Figure 5. Distribution of the effective radius of bulge (Re_{bulge}) and disk (Re_{disk}) across F150W, F200W, F277W, F356W, F410M, and F444W, with the red and dark blue dotted vertical line indicating the median of the effective radius of the bulge and the disk respectively.

65.0% (25/40) in F444W with $n_{bulge} = 0.68$ ($\sigma = 1.49$), compared to only 12.8% (6/47) in F150W with $n_{bulge} = 1.06$ ($\sigma = 0.67$).

We also have to consider the

In brief, the bright SMGs maintain similar Sérsic indices of the bulge, while still having higher B/T than the faint SMGs. All of these patterns highlight a structural gradient tied to both wavelength and flux.

4.1.3. Properties of the SMGs in different bulge categories

We highlight the properties of our sample of SMGs categorized by different types of bulges in Table 5. Classical bulges exhibit relatively high stellar mass ($1.6^{+1.1}_{-0.9} \times 10^{11} M_{\odot}$) and elevated star formation rates ($162.2^{+200.9}_{-73.1} M_{\odot} \text{ yr}^{-1}$). In particular, they show some of the broadest diversity in structural properties, with a bulge-to-total ratio (B/T) of $0.3^{+0.2}_{-0.1}$, a Sérsic index of $n = 4.6^{+1.1}_{-1.9}$, and an effective radius of $R_{\text{eff}} = 2.0^{+0.0}_{-0.5} \text{ kpc}$.

Within this category, bulges built through major mergers are sites of particularly extreme cases. These systems have high stellar masses ($1.3^{+1.3}_{-0.9} \times 10^{11} M_{\odot}$) and SFRs ($152.5^{+273.6}_{-116.6} M_{\odot} \text{ yr}^{-1}$), along with the highest median B/T ($0.6^{+0.1}_{-0.0}$), a high Sérsic index ($n = 4.4^{+1.0}_{-0.2}$), and compact bulges ($R_{\text{eff}} = 1.4^{+0.7}_{-0.1} \text{ kpc}$).

Clump-sinking bulges have stellar masses similar to average classical bulges ($1.6^{+0.6}_{-0.4} \times 10^{11} M_{\odot}$) and even higher SFRs ($204.4^{+294.2}_{-95.5} M_{\odot} \text{ yr}^{-1}$). Structurally, they lie between merger-built bulges and pseudobulges: their B/T is $0.5^{+0.1}_{-0.1}$, Sérsic index is $2.7^{+0.6}_{-0.3}$, and effective radius is $2.0^{+0.1}_{-0.6} \text{ kpc}$.

Pseudobulge-hosting SMGs exhibit the lowest median stellar mass among the classified categories ($0.8^{+0.4}_{-0.4} \times 10^{11} M_{\odot}$) and slightly lower SFRs ($151.4^{+137.1}_{-122.5} M_{\odot} \text{ yr}^{-1}$). Morphologically, they have the lowest B/T ($0.1^{+0.1}_{-0.1}$), lowest Sérsic indices ($n = 1.4^{+0.8}_{-0.6}$), and relatively compact bulges ($R_{\text{eff}} = 1.1^{+0.6}_{-0.1} \text{ kpc}$).

Finally, SMGs with unclassified bulges show moderate stellar masses ($0.9^{+0.9}_{-0.6} \times 10^{11} M_{\odot}$) and the lowest SFRs ($128.8^{+153.3}_{-52.0} M_{\odot} \text{ yr}^{-1}$). They exhibit the lowest Sérsic indices ($n = 0.7^{+0.2}_{-0.0}$), intermediate B/T ($0.7^{+0.2}_{-0.2}$), and modest bulge sizes ($R_{\text{eff}} = 1.6^{+0.3}_{-0.3} \text{ kpc}$).

4.2. Non-parametric metrics

Beyond Sérsic fitting, we examine the morphology of SMGs using the CAS systems (C, A, S), and the $Gini - M_{20}$ metrics across F150W-F444W, leveraging F277W as the benchmark for non-parametric analysis, since the parametric fitting cannot fully disclose the morphological information, especially for clumpy discs and SMGs with merger signatures. We follow the identical categorization above based on SFR, on the basis of

which we present the distribution of the non-parametric metrics. We checked the results and ensured the results robust estimations (`flag = 0`), yielding 101 SMGs with high-quality results. An detailed table with non-parametric metrics is shown in the Appendix Fig 11.

For CAS systems, faint SMGs(61/101) show a median concentration $C = 2.78$ and asymmetry $A = 0.18$, painting a picture of compact, smooth, nearly featureless disks. However, bright SMGs(40/101) shift to lower concentration but higher asymmetry, with $C = 2.75$ and $A = 0.21$, suggesting a more disturbed inner structure than their fainter counterparts. We then perform the KS test and the result indicates that there is no significant difference between these two groups despite the marginal difference in concentration and asymmetry, suggesting an overall uniformity across the 2mJy threshold in these measures.

To probe the origin of the SMGs derived from morphological information, we then inspect the Gini- M_{20} plot, which is shown in Fig 6. The overall merger rate of our sample SMGs is 24%. For faint SMGs, the median is $Gini = 0.51$ and $M_{20} = -1.55$, while the median is $Gini = 0.50$ and $M_{20} = -1.50$ in bright SMGs. KS test again suggests similarity (with $p = 0.67$ for Gini, $p = 0.49$ for M_{20}), with most SMGs clustering in the disk region. Still, 24%(24/101) falls into the merger zone(27.5% bright, 8/40, and 21.3% faint, 13/61), consistent with the minor dynamical disturbance. Additionally, the M_{20} , which tracks the degree of separation of distribution of luminous clumps within the boundaries of the galaxies, shows better separation in distinguishing the bright population from the faint ones than all the other non-parametric indices including Gini. This phenomenon has been confirmed in B. Nevin et al. (2019). Our sample have a broad redshift range, spanning from $z \sim 1 - 6$, which corresponds to rest-frame wavelength range of $\sim 0.4 - 1.39\mu m$ in band F277W, with the median $0.84\mu m$ (16th-84th percentile: $0.57 - 1.12\mu m$), spanning from optical to near-IR regime. Despite previous studies showing the variations in the rest-frame wavelength may affect the measurements of M_{20} (J. Ren et al. 2025b), we find no significant statistical differences by performing the KS test (p-value=0.19) on the M_{20} value between the two groups divided by $0.75\mu m$. Additionally, the offset between the two groups is modest ($\Delta M_{20} = 0.07$), with median $M_{20} = -1.48$ for the $< 0.75\mu m$ group and median $M_{20} = -1.55$ for the $> 0.75\mu m$ group. Consequently, the impacts due to variations of the rest-frame wavelength are limited in this work.

The overall non-parametric metrics echo the results of parametric light distribution modellings, reinforcing

the idea of prevalence of disk structures and internally driven scenarios in the SMGs population from previous studies.

5. DISCUSSION

5.1. Pseudo-bulge or Classical Bulges?

First of all, before diving into detailed discussions, we must clarify the definition of the classical bulges and pseudobulges, which are sometimes quite ambiguous to elucidate. In general, they are distinguished by their assumed formation mechanisms: pseudo-bulges are thought to arise from gas inflows triggered by their bars or spiral arms within the disc plane, or any internal processes, whereas the classical bulges are often attributed to the violent relaxation induced by either the local disk instability or the major mergers. However, this theoretical divide crumbles under scrutiny, as observational diagnostics to confirm such origins remains scarce, especially at high redshift.

For example, several early simulations show that massive star-forming clumps in gas-rich, high-redshift discs can merge into the central structures resembling dispersion-dominated classical bulges owing to dynamical frictions, with α -enhanced abundances and the $R^{1/4}$ light distribution (A. Immeli et al. 2004; B. G. Elmegreen 2009; M. Noguchi 2000), while some others show that the majority of clumps at high-redshift, gas-rich disks are short-lived and gravitationally unbound, which dissipate before entering the center of the galaxy, making it unclear to fully explain it being the sole origin of the classical bulge at high redshift, gas-rich galaxies (X. Meng & O. Y. Gnedin 2020; A. Oklopčić et al. 2017).

On the observational side, previous work on the 'cosmic grape' (S. Fujimoto et al. 2024) reveals the fact that numerous star-forming clumps are formed through the disk instabilities with weak feedback effects, suggesting in situ formation of clumps in high redshift, gas-rich, rotating disks. Another study shows that there is a statistically significant correlation between clumpiness and the bulge-to-disc flux ratio (B. S. Kalita et al. 2024), strongly suggesting that bulges are evolutionarily related to clumps. In addition, some models suggest such bulge should have lower Sérsic index and significant rotation, correlating to the bar (P. F. Hopkins et al. 2012; K. Saha et al. 2016; S. Inoue & T. R. Saitoh 2012). Yet, the conventionally accepted notion of the formation of classical bulges is bound to major merger activity, and these clump-built structures need further confirmation, despite being observationally similar.

We set our boundaries for classical bulge and pseudobulge based on the list of the classical-pseudobulge classification criteria, provided in John Kormendy arti-

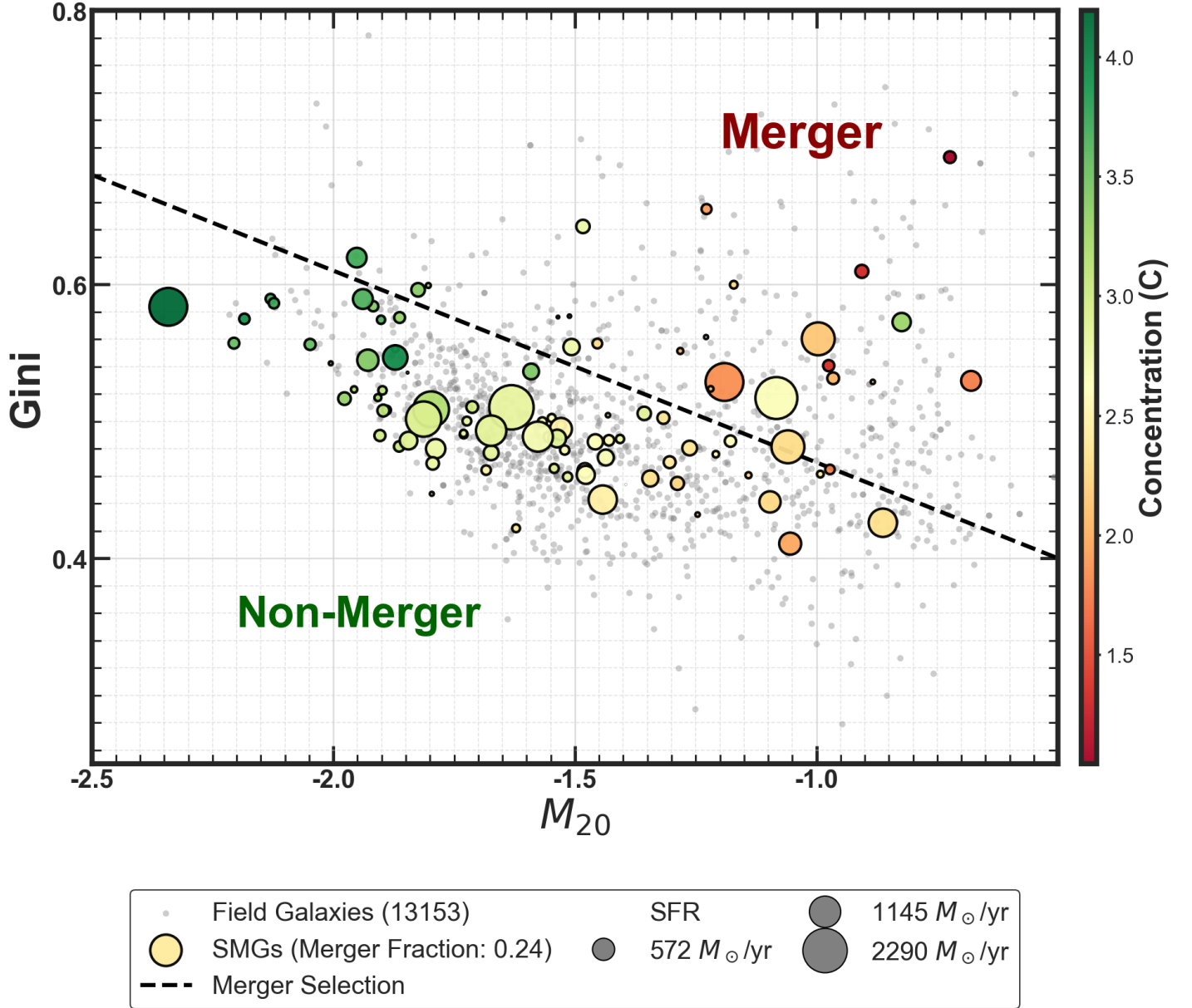


Figure 6. Gini- M_{20} relation for both the SMGs and the field galaxies in the PRIMER-COSMOS field, with the dashed line indicating the boundary of the galaxies with merger signatures and those non-mergers, with detailed description in [J. M. Lotz et al. \(2008\)](#).

cle([J. Kormendy 2016](#); [J. Kormendy & R. C. Kennicutt 2004](#); [J. Kormendy & R. Bender 2012](#)), in which contains detail distinctions between these two structures, including the morphological properties, abundance of metallicity, and velocity field etc. We only take the standards regarding the Sérsic index and bulge-to-total luminosity ratio (B/T), owing to the limitation of our data. The followings are our standards:

- Classical Bulge(General Classification):

- $n \geq 2$

- $B/T > 0.2$ (Optional, for more restricted purpose)

- Classical Bulge(Merger-built):

- $n \geq 4$

- $B/T > 0.5$

- Classical Bulge(Clump sinking):

- $2 < n < 4$

- $B/T > 0.2$ (Optional, for more restricted purpose)

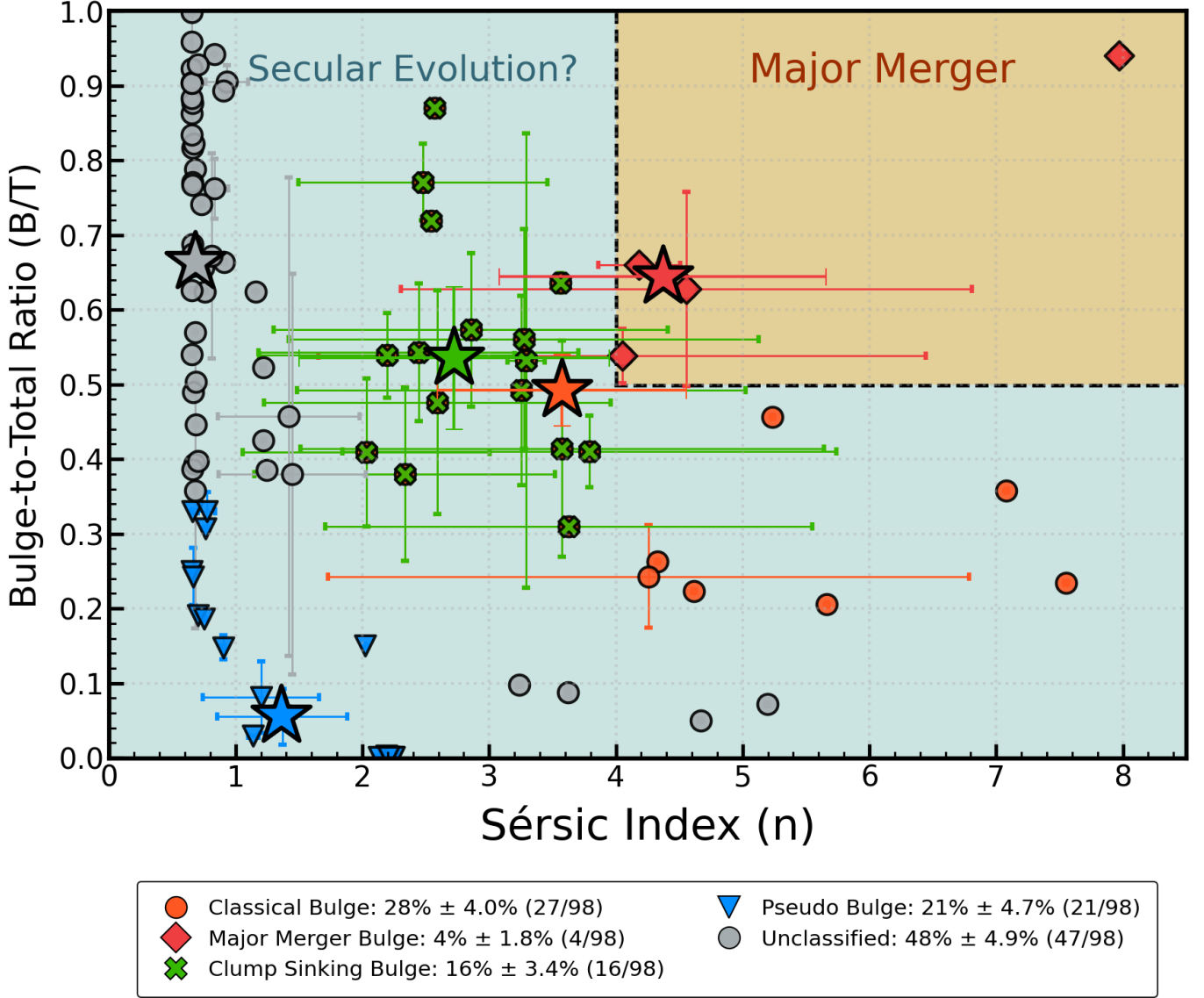


Figure 7. The distribution of different types of bulges based on the classification scheme using sérsic index and bulge-to-total luminosity ratio on band F277W after the removal of the strongly disturbed SMGs , with the big star symbols showing the median of each group.

- Pseudobulge(General Classification):

- $n < 2$
- $B/T \leq 0.35$

and please keep in mind that each of these classification criteria has its failure rate ranging from 0% to 20%. To make it clear , there is no absolute standard in these two types of structure and the classification scheme is for rough reference only.

We then use the standard above to gauge the number of each category in the F277W band due to the completeness of the image data , and it turns out to be quite intriguing. The results are shown in Fig. 7. After

removing the SMGs with strongly disturbed morphology(majority of the removals are identified as 'merger' and 'clumpy' , but not necessarily all of them) by visual inspection , the number of general classification of classical bulge yields 40 out of 98 , and 27 out of 98 with a more rigorous version. For the pseudobulge , the classification shows 21 out of 98 bulges that are qualified for the selection criterion. Additionally , there are only four merger-built classical bulges , whereas 36 of the bulges are certified as the classical bulge built via clumps sinking(16 out of 98 for more rigorous purpose). Interestingly , half of the bulges(47/98) fail to fall into any of our categories , with the vast majority clustering around the area where the higher B/T and lower Sérsic

coexist , suggesting that the majority of the bulge components in the higher redshift SMGs are still in a phase of growth and becoming more and more prominent.

We have mentioned in the previous section that SMGs in our sample tend to have higher B/T and lower Sérsic index at the same time , while lower B/T and higher Sérsic index simultaneously , which contradicts the paradigm that a classical bulge must have higher B/T plus higher Sérsic index and a pseudo-bulge must have lower B/T and lower Sérsic simultaneously. The p -values shown in Table 2 suggest no significant statistical difference between the two SFR splits in all morphological parameters. In addition , there is a decreasing trend in the Sérsic index in both $< 175M_{\odot} \text{ yr}^{-1}$ and $\geq 175M_{\odot} \text{ yr}^{-1}$ group , which is more evident in the bright population. This suggests the fact that the bulges in the SMGs have an extended , disk-shaped geometry , similar to local pseudobulges in terms of Sérsic index but having a much larger B/T value. The trend confirms that the bulge component is more prominent in the longer wavelength , revealing a wavelength-dependent effect possibly tied to dust penetration.

The physical sizes of both bulges and disks in all six of these JWST bands show no significant statistical difference by implementing the KS test, although the physical sizes of the bright group are slightly larger than their fainter counterparts(e.g., median $R_e \sim 6.28kpc$ (bright) vs. $4.81kpc$ (faint) in band F115W). This compactness challenges the notion that classical bulges , if merger-induced , should expand markedly while still dominating the luminosity of the galaxies. Instead , the prevalence of pseudobulge , clump-sinking bulges , plus unclassified bulge with high B/T ($\sim 90\%$) and the modest merger fraction(24%) point toward a secular evolution scenario , where gas-rich discs at high redshift foster in situ bulge formation through violent disk instabilities(A. Dekel et al. 2009). On top of that , we have mentioned in the previous section that there is a subgroup with high Sérsic index but lower B/T , in other words , the small classical bulge. This type of bulge is considered to be the product of minor mergers or clumps migration(J. Kormendy 2016; K. Saha et al. 2012; O. A. Gonzalez & D. Gadotti 2016; F. Combes 2016) , some of which in the local universe are also embedded in the pseudobulge driven by bar instability(P. Erwin et al. 2015) , making the whole a composite bulge. In addition , C. E. Benton et al. (2024) shows that bulge formation starts prior to the quiescence phase , imposing new constraints on the evolution pathways of the high- z star-forming galaxies.

However, Q.-H. Tan et al. (2024) points out that the in-situ formations of spheroids in submillimeter-bright galaxies (SMGs) are induced by mergers, lever-

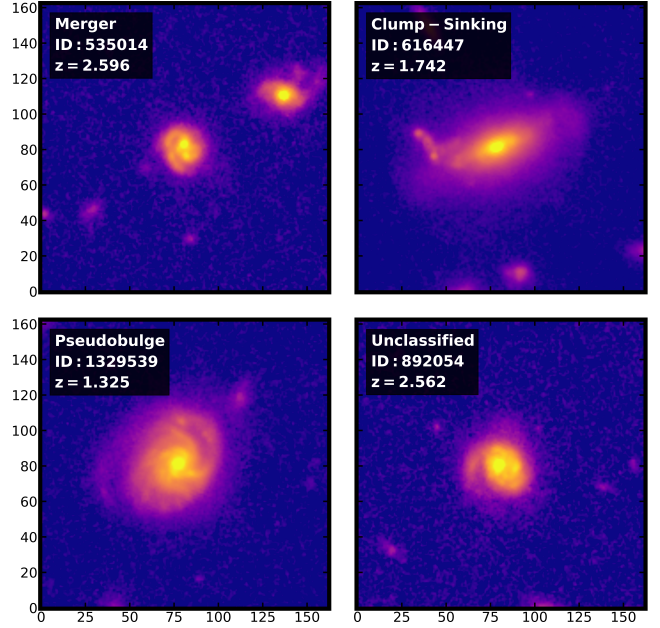


Figure 8. Example of SMGs with different bulge type , including merger-built bulge , clump-sinking bulge , pseudobulge , and unclassified bulge.

aging high-resolution ALMA observations of 146 bright SMGs($S_{870\mu m} = 7.8mJy$, $\log(M_*/M_{\odot}) = 11.0$, $SFR = 624M_{\odot}yr^{-1}$) in COSMOS and GOODS-S fields and being supported by simulations. Morphologically, they show bulge-like profiles (median Sérsic index ($n \approx 1.6$), spiegel index ($v = -0.26$)) and triaxial shape($q = 0.71$, $C/A = 0.53$). Combined to our sample(which is less intensive SMGs, merger-rate being 27.5% in bright group, and 21.3% in faint group via non parametric methods), still, secular evolution takes precedence over major mergers, albeit merger being more prominent in the formation of brigher, more intense SMGs.

Despite the theoretical and observational constraints above , we must clarify the possibility that these outcomes could be merely mathematical manifestations of the model without substantial physical interpretation. For instance , half of the SMGs have a bulge with high B/T (~ 0.7) but low Sersic(~ 1) , with B/T accuracy spanning $91.2\%^{+6.5}_{-60.1}$, which may denote that B/T is unstable, indicating that the single sérsic profile suffices to describe the light distribution of the SMGs at high redshift , with the possibility of the absence of bulges inside the SMGs at high- z , or the nucleus is still in the process of formation.

With all regarded , the traditional dichotomy of pseudo-bulge and classical bulge shows limitations under the influence of gas dynamics and dust at high redshift , rendering SMGs as a possible hybrid class required further observational constraints.

5.2. Origin of SMGs: Merger-induced or Internally Driven?

As shown in Figure 6, we show the Gini- M_{20} plot of the SMGs sample in F277W, split by two flux bins following the identical configuration as the one above. It is evident that the majority of SMGs(90/101) lie in the non-merger region. In either the faint or bright group, SMGs with higher star formation rate(as marked by the size of the scatter point) tend to reside in the area of late-type galaxies, which is basically composed of disc and irregular galaxies, suggesting that the intense starburst activities occur in the non-merging phase (or pre-merging phase, if the major merger origin is validated, referring to the evolution pathway of Gini and M_{20} in this hydrodynamical simulation A. Calabrò et al. (2019) for details), consistent with starburst systems driven by internal dynamics(C. M. Casey et al. 2014).

Besides that, our nonparametric metrics in previous section paint a different picture from the major-merger-induced scenario. In F277W, the Gini and M_{20} remain relatively stable across flux bins, with p-value(> 0.05) indicating no significant structural shifts. The concentration($C \sim 2.75$) and asymmetry($A \sim 0.20$) indices further underscore settled, less disturbed disk-like systems, consistent with those intense starburst systems in C. J. Conselice (2014). The morphological outcomes align with multiple previous studies. J. A. Hodge et al. (2025), using high resolution ALMA 870 μm imaging, finds out that SMGs at $z \sim 2 - 3$ exhibits disk-like feature($n = 1$) though measurements of compact star forming regions($R_e = 0.6 \text{ kpc}$) as well as clumpy sub-structures supporting an in-situ star formation via violent disk instabilities. Similarly, S. Fujimoto et al. (2018) demonstrates that dusty star-forming galaxies with far-IR luminosities($L_{IR} = 10^{11} - 10^{13} L_{\odot}$) present disk-like morphology and compact far-IR emission areas($R_{e,FIR} \sim 1 \text{ kpc}$), indicating starbursts in gas-rich disks.

A. Le Bail et al. (2024) provide a new dynamical framework for dusty star-forming galaxies(DSFGs), in which lopsidedness in 64 % of the DSFGs is primary driven by asymmetric gas accretions and secondarily driven by minor mergers. Despite some impacts on lopsidedness, major merger is just a case-by-case basis and shows no statistical significance. Additionally, the study finds galaxies with high lopsidedness residing in isolated environment, suggesting it being an internal dynamical process. Accretion-induced lopsidedness facilitates violent disk instability, forming clumps that migrate inward to build diffuse extended disk-like bulge secularly while maintaining high SFRs(A. Dekel et al. 2009). This accounts for our low asymmetry and high

concentration, as the VDI maintains disk-like morphology.

Only 24%(24/101) of the SMGs fall in the merger region, with bright(27.5%) groups having slightly higher merger-rate than the faint group(21.3%), a fraction which is too modest to drive the bulk of our sample's star formation. This aligns with the S. Fujimoto et al. (2018) merger fraction in ULIRGs and the J. A. Hodge et al. (2025) $\sim 16\%$ merger signatures, indicating an enhancements in star formation from mergers in luminous SMGs. A. Le Bail et al. (2024) notes that the minor merger boosts the lopsidedness, triggering disk instabilities(S. Gillman et al. 2024) and gas inflows to the center and forming a compact core, which aligns with our finding of small classical bulges.

The data points towards an internally driven scenario, where gas-rich discs at high redshift sustain starbursts through violent disk instability rather than extreme merger activities(A. Dekel et al. 2009). The transient, "pre-merger" stage inadequately explains our SMGs' persistent disk-like feature and high star formation rate throughout the non-merger phase, if the merger-origin doctrine is valid. Instead, the observed clumps and gas compression may arise in situ, fueled by the filamentary inflows, with mergers playing a secondary role, which is decent in the sense that a denser, more gas-rich environment in the early universe can yield the starburst activity with comparable star formation rate like the local ULIRGs, which are typically associated with major mergers(A. R. Draper & D. R. Ballantyne 2012; M. Pereira-Santaella et al. 2021; M. Perna et al. 2021, 2022), but through smaller scale internal dynamical process. The internal structure, such as the bulge, disk, and stellar bar, can be fabricated through internal gas compressions and manifest the intrinsic spin of the dark matter halo, which is supported by several recent simulations(M. Du et al. 2021; H.-C. Ma et al. 2024; S. Lu et al. 2025). The observations of the JWST reveal modest evidences against the idea of formation of SMGs induced by major merger, pointing to the fact that the formation mechanisms of these high- z dusty star-forming systems lean heavily on internal dynamics, with external interaction enhancing, rather than initiating, their evolutionary pathway.

5.3. Visual Morphology and Stellar Bar

Thanks to the advent of the James Webb Space Telescope(JWST), we are now able to visually inspect hidden details behind those dusty facades of the SMGs, with unprecedented high sensitivity and spatial resolution. Still, we perform the visual inspections on the SMGs in band F277W due to the completeness of the im-

age data , with the rest-frame wavelength spanning from the optical to near-infrared regime($0.84^{+0.28}_{-0.27} \mu m$). We find that $\sim 34\%$ of the SMGs exhibit clear undisturbed disk-like morphology and $\sim 22\%$ with clumpy feature. The majority of the remaining SMGs has smooth , flat-ten morphology, except for the minority displaying the merger signatures($\sim 20\%$). Within the disk group , $\sim 66\%$ features apparent spiral arms and $\sim 43\%$ has stellar bar(5 confirmed bar + 13 tentative candidates). We then visually check the residuals of the Sérsic fittings to ensure credibility and reliability of bar detection , producing 9 (9/43 , $\sim 21\%$ within the disk-like group) SMGs with a strong , confident bar-like structure that facilitate gas accretion funneling into the center of the galaxy, with the residuals shown in Appendix 12. All of the bar candidates are all clustered at $z \sim 1-3$, peaking at $z \sim 2$. Yet , the fraction of the total bar candidates could be underestimated because of the high inclination and the faint detections. Interestingly , we notice that several of our edge-on SMGs have traces of filamentary gas accretion , and the other two exhibit point source features , indicating potential AGN activities.

The stellar bar plays a significant role in galaxy evolution , such as driving the internal processes , triggering gas inflows , forming boxy/peanut-shaped structures , influencing AGN fuelings , indicating evolutionary stage , redistributing baryonic matters , etc. J. McKinney et al. (2025) shows $8\% \pm 3\%$ of the SMGs with confirmed bar-like features, which is in agreement with our findings($\sim 7\%$). All things considered, it is highly probable that the formations of structures such as stellar bars, spiral arms , and bulges are in situ , caused by internal gas compressions, rather than external interferences.

6. CONCLUSIONS

In this study , we leverage the high resolution and precision of the James Webb Space Telescope(JWST) NIRCam imaging to probe the morphology of 125 $z \sim 1-6$ SMGs in the PRIMER-COSMOS field. All of our SMGs have robust detections of ALMA , with all of the physical properties presented in this paper retrieved from the A3COSMOS catalogue (S. Adscheid et al. 2024). The followings are our primary findings:

- Secular Evolution as primary mechanisms: Morphological analysis of 125 ALMA-detected submillimeter galaxies(SMGs) in the PRIMER-COSMOS field , using the JWST/NIRCam imaging(F150W, F200W, F277W, F356W, F410M, F444W) , shows 76% of the SMGs with a disk-like structure , which is potentially driven by secular evolution via violent disk instabilities and fil-

amentary gas inflows , which challenge the major merger-dominated paradigm.

- SFR-dependent morphology: Besides being intrinsically different at the stellar mass and the star formation rate , double sérsic modellings reveal bright SMGS have higher bulge-to-total luminosity ratio($B/T = 0.60 \pm 0.05$) and lower bulge Sérsic index($n_{bulge} = 0.91 \pm 0.27$) than the fainter one($B/T = 0.52 \pm 0.04$, $n_{bulge} = 1.58 \pm 0.18$) in band F444W , suggesting varying degrees of internal evolution and different formation pathway.
- Disk-Dominated Structures: Non-parametric metrics in band F277W for 101 SMGs yield low asymmetry and the higher concentration($A = 0.19^{+0.09}_{-0.07}$, $C = 2.77^{+0.40}_{-0.38}$) , with the majority of our samples falling in the non-merger region , aligning with that of disk-dominated starburst group. Only 24% shows merger signatures , consistent with 16–21% merger rate from S. Gillman et al. (2024) , S. Fujimoto et al. (2018) , and J. A. Hodge et al. (2025).
- Bulge formation and Hybrid-origin Model: Bulge classification yields 16% of SMGs with clump sinking bulge($2 < n_{bulge} < 4$, $B/T > 0.2$) and 4% merger-built bulge. 48% (47/98) of our sample have unclassified bulges , with the vast majority showing high B/T (~ 0.7) but low Sérsic indices ($n_{bulge} \sim 0-1.2$) , suggesting ongoing VDI-driven bulge formation. This supports a secular evolution model: 79% secular , 21% minor merger-induced lopsidedness (A. Le Bail et al. 2024).
- Visual Morphology : JWST/NIRCam imaging shows that 34% of 125 $z \sim 1-6$ SMGs in the PRIMER-COSMOS field have disk-like structures along with spiral patterns and stellar bars that are either confirmed or tentative (5 confirmed , 13 tentative). Clumpy features in 22% of the SMGs indicate violent disk instability (VDI)-driven star formation while 20% show signatures of mergers and the remaining objects exhibit smooth flattened profiles. Sérsic fitting residuals reveal 9 SMGs in 21 percent of disk systems that exhibit strong barred structures potentially driving starburst activity at their centers. Several edge-on SMGs display filaments of gas which confirms VDI yet two other SMGs contain point-like features that point to AGN activity.

Our work demonstrates the dominance of the internally driven secular evolution framework for the formation pathways of the SMGs , while mergers play a

secondary role. However, stellar bar, or any other substructures of the inner part of the galaxies have not been ruled out while performing double Sérsic light distribution modellings, which requires further scrutinizations. More precise, in-depth studies via spectroscopic methodologies with ALMA and JWST will be crucial to probe the kinematics nature, constrain clump masses, and confirm AGN activity, shedding light on the dynamics of these high- z , dusty starburst systems.

ACKNOWLEDGEMENTS

We appreciate comments from the anonymous reviewer which improve the quality of this work. We also extend our gratitude to Luis C. Ho and Daizhong Liu for providing insightful advice that expands the scope and depth of this work. Y.A. acknowledges the support from the National Natural Science Foundation of China (NSFC grants 12173089), the Strategic Priority Research Program of the Chinese Academy of Sciences (Grant No.XDB0800301), and the National Key R&D Program of China (2023YFA1608204). This work is based on observations made with the NASA/ESA/CSA James Webb Space Telescope. The data products presented herein were retrieved from the Dawn JWST Archive (DJA). DJA is an initiative of the Cosmic Dawn Center (DAWN), which is funded by the Danish National Research Foundation under grant DNRF140.

Software: Astropy([Astropy Collaboration et al. 2013, 2018, 2022](#)), Matplotlib([J. D. Hunter 2007](#)), Photutils([L. Bradley et al. 2024](#)), Pysersic([I. Pasha & T. B. Miller 2023](#)), Statmorph([V. Rodriguez-Gomez et al. 2019](#)), Topcat([M. Taylor 2017](#)), Grizli([G. Brammer 2023](#))

APPENDIX

A. DISTRIBUTION OF THE BULGE SÉRSIC INDICES BY B/T BINS AND SINGLE SÉRSIC , AND NON-PARAMETRIC RESULTS DIVIDED BY STAR FORMATION RATE

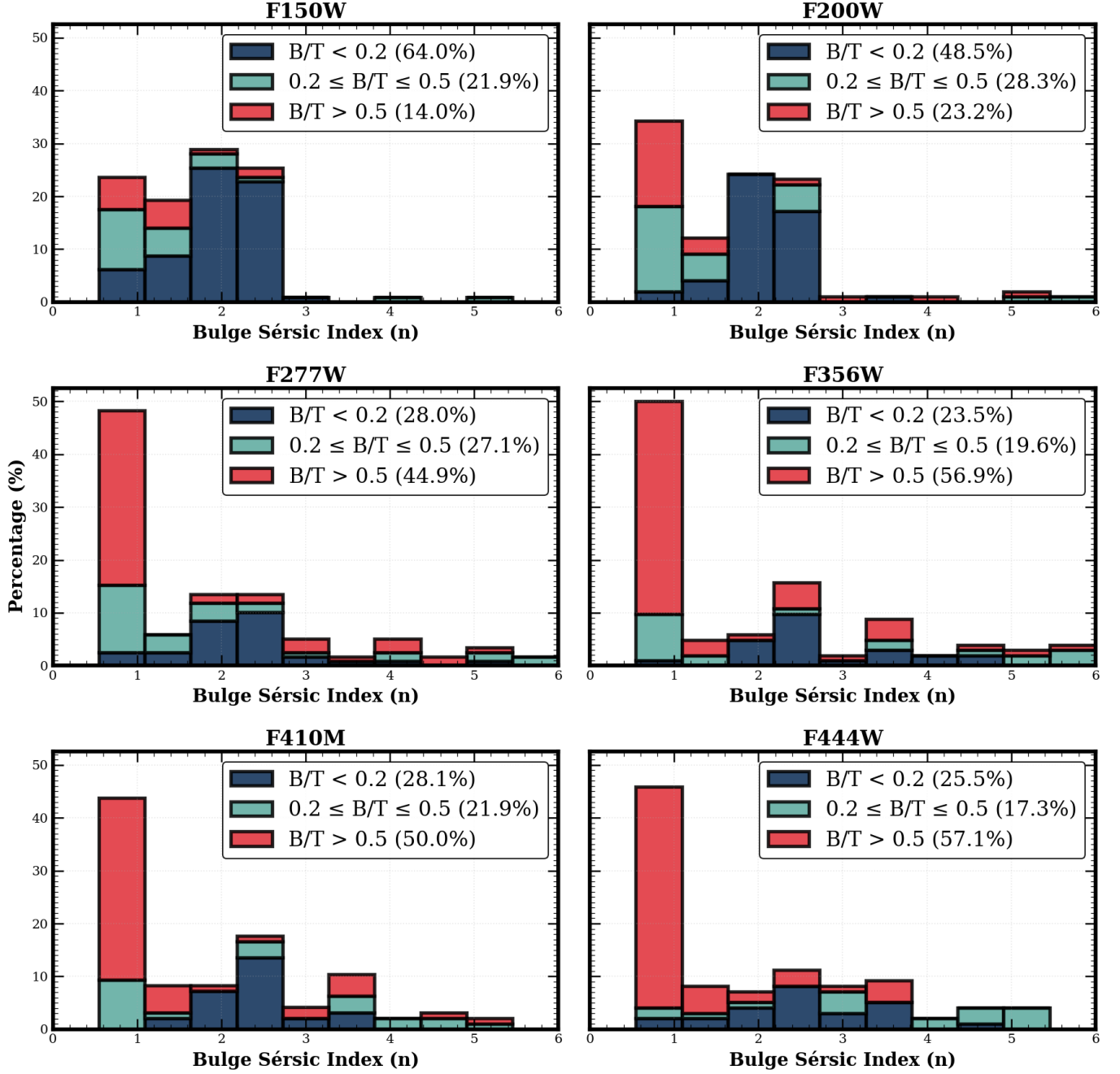


Figure 9. The distribution of the bulge Sérsic index across six band(F150W, F200W, F277W, F356W, F410M, F444W) divided by three B/T bins($B/T < 0.2$, $0.2 < B/T < 0.5$, $B/T > 0.5$).

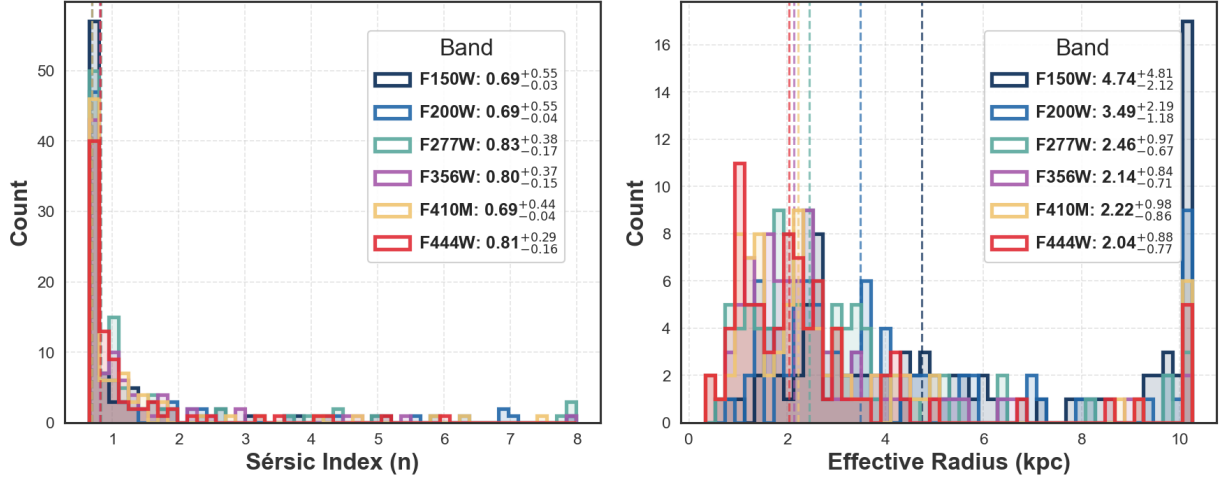


Figure 10. Results of the single Sérsic fitting: Distribution of Sérsic index and effective radius for JWST bands.

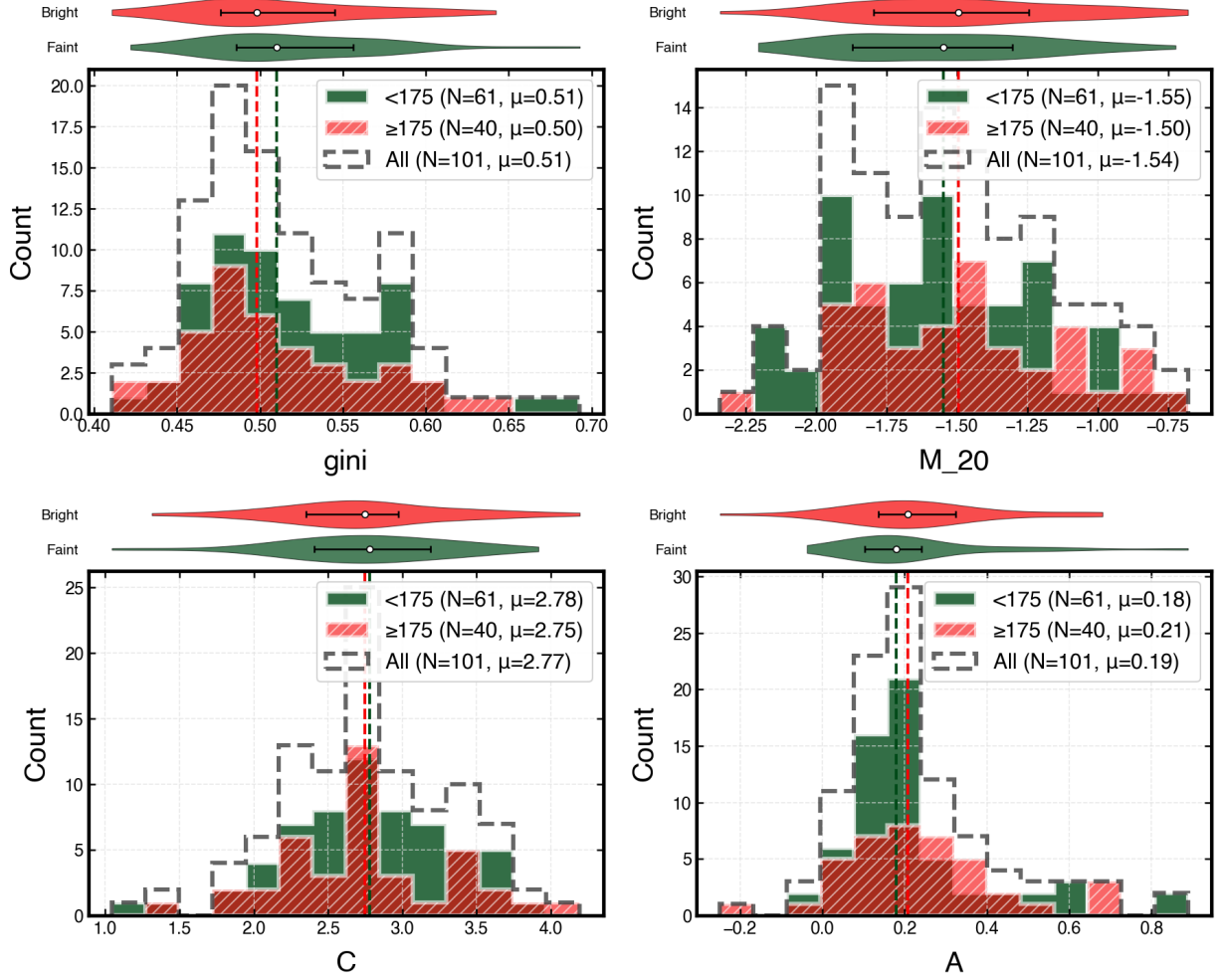


Figure 11. The non-parametric metrics of the bright (SFR > 175 $M_{\odot} \text{ yr}^{-1}$) and faint group (SFR < 175 $M_{\odot} \text{ yr}^{-1}$), marked by red and dark green respectively.

B. BAR IDENTIFICATION BY RESIDUALS OF SINGLE SÉRSIC FITTING

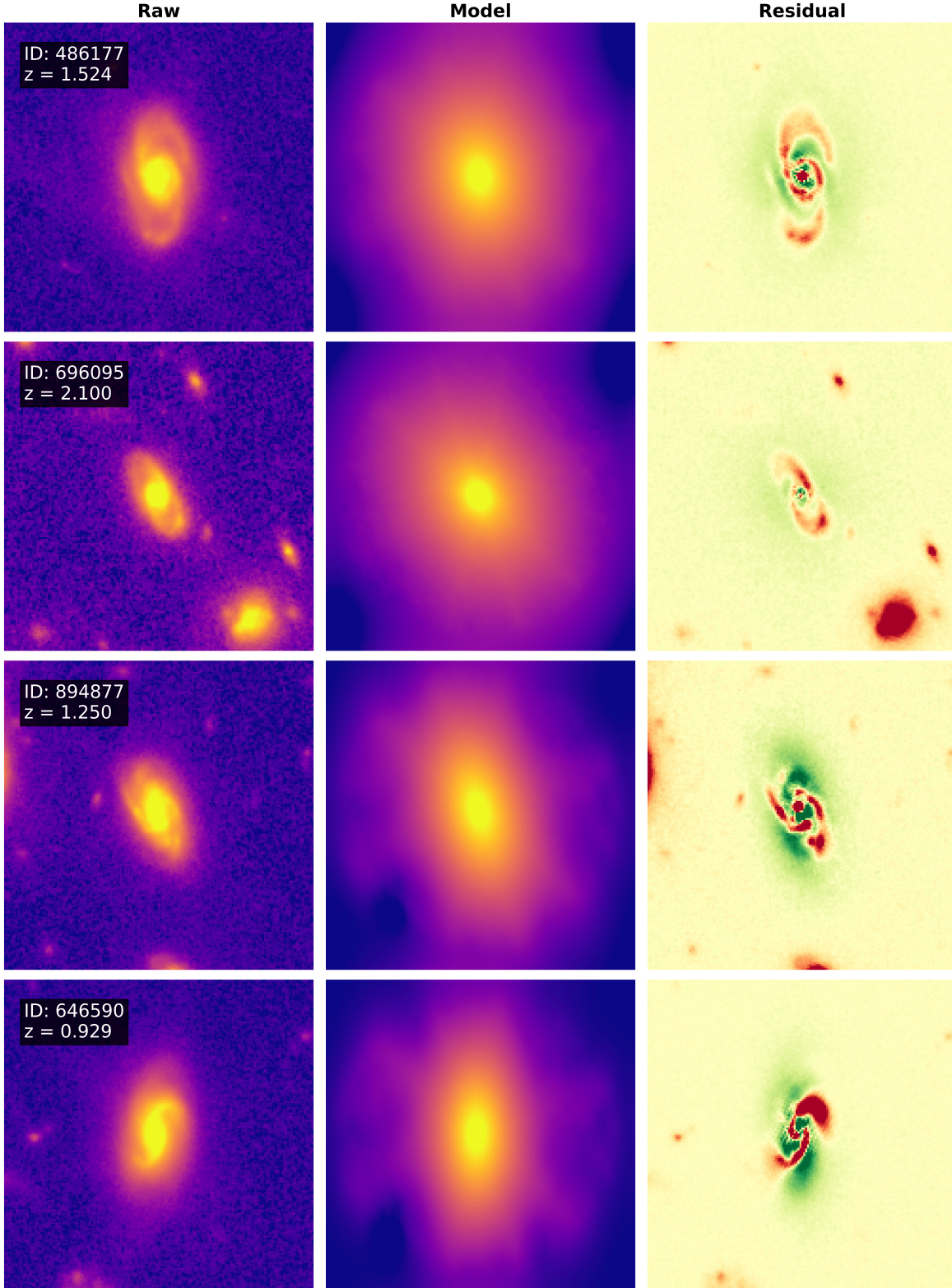


Figure 12. The confirmed bar candidates using the residuals of the single Sérsic fitting in band F277W. Each image is $6.5'' \times 6.5''$.

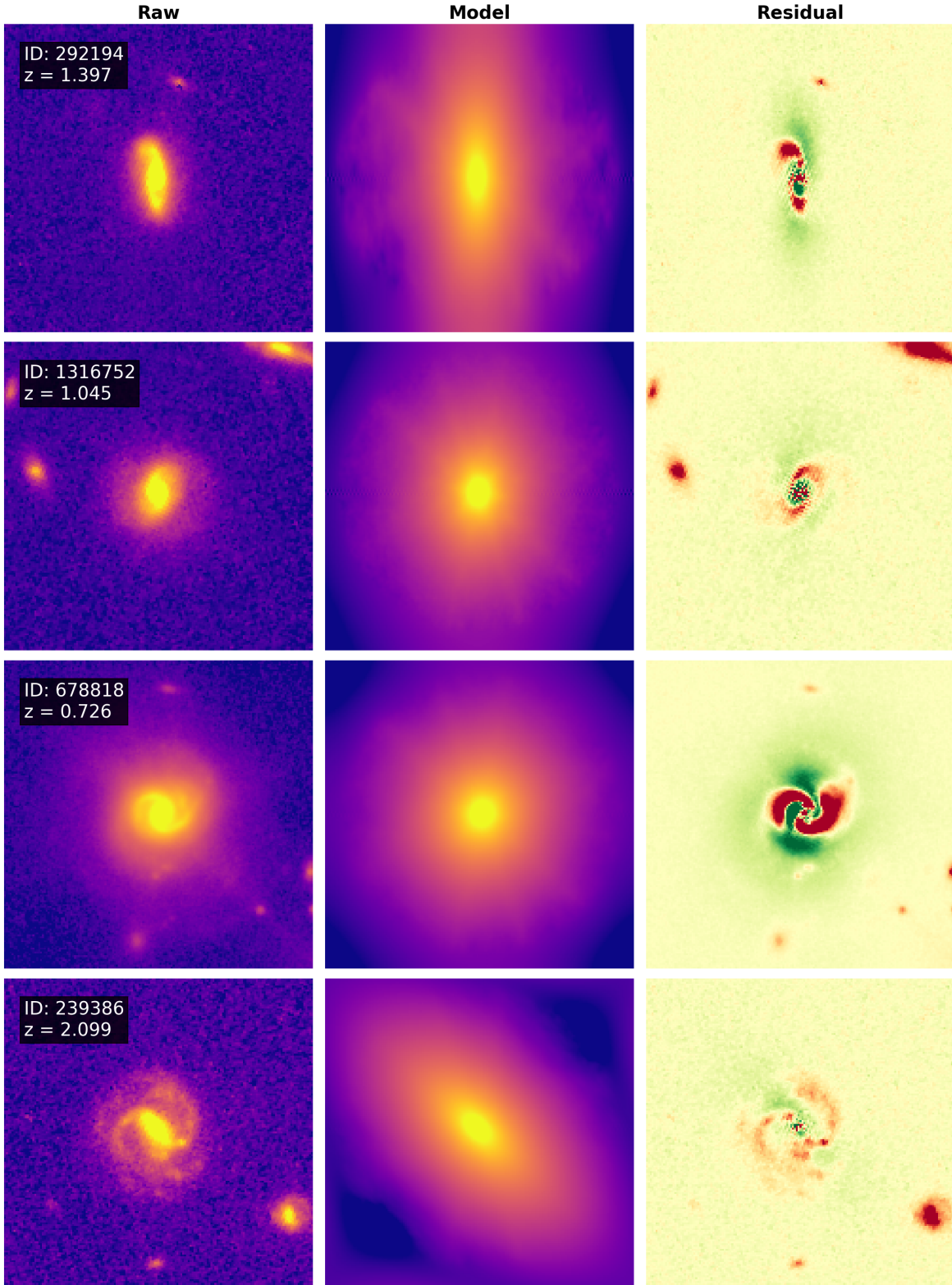


Figure 12. Continued.

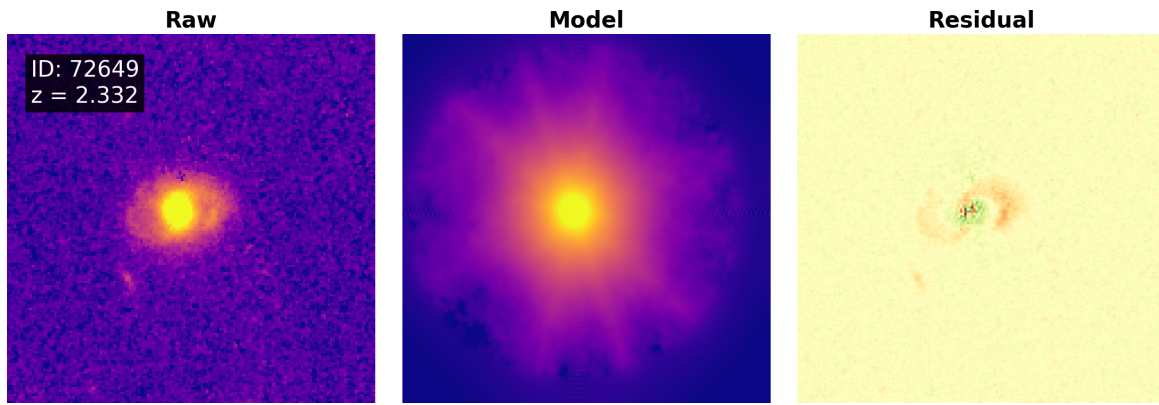


Figure 12. Continued.

C. PHYSICAL PROPERTIES AND COORDINATES

Table 6. The catalog containing SMGs in the PRIMER COSMOS field with ALMA (A3COSMOS) physical properties and coordinates, alongside JWST (DJA) coordinates.

ID	ALMA (A3COSMOS)							JWST (DJA)	
	RA [deg]	Dec [deg]	z	$\log_{10}(M_*/M_\odot)$ [dex]	$\log_{10}(L_{\text{dust}}/L_\odot)$ [dex]	SFR [$M_\odot \text{ yr}^{-1}$]	sSFR [yr^{-1}]	RA [deg]	Dec [deg]
21931	150.11252	2.37655	1.92	11.77	12.22	165.96	0.28	150.11253	2.37654
41140	150.18004	2.37828	4.91	10.45	12.65	446.68	15.85	150.18011	2.37831
43882	150.07724	2.21141	2.18	11.06	11.72	52.48	0.46	150.07725	2.21141
56056	150.10282	2.37939	1.85	11.49	11.96	91.20	0.30	150.10285	2.37940
58907	150.07527	2.37943	2.00	10.88	11.86	72.44	0.96	150.07525	2.37941
72649	150.18711	2.38011	2.33	11.38	12.06	114.82	0.48	150.18717	2.38014
74827	150.13265	2.21185	2.11	11.62	13.10	1258.93	3.02	150.13266	2.21185
75594	150.14361	2.47353	0.51	8.00	8.61	0.04	0.41	150.14361	2.47355
77591	150.07574	2.38074	2.47	10.44	11.84	69.18	2.51	150.07584	2.38072
77714	150.07715	2.38034	2.92	11.06	12.11	128.83	1.12	150.07717	2.38037
82551	150.07594	2.21182	2.10	11.66	12.59	389.05	0.85	150.07595	2.21181
83665	150.17324	2.46432	1.75	11.12	12.30	199.53	1.51	150.17325	2.46432
86289	150.12178	2.21323	1.41	10.76	12.03	107.15	1.86	150.12179	2.21322
97487	150.15865	2.46835	6.50	10.97	13.00	1000.00	10.72	150.15859	2.46835
110346	150.16768	2.29873	2.09	11.54	12.26	181.97	0.53	150.16768	2.29875
119950	150.10284	2.38455	1.95	11.23	12.02	104.71	0.62	150.10283	2.38451
163763	150.03669	2.21790	1.82	11.71	12.36	229.09	0.45	150.03670	2.21788
163962	150.18404	2.38637	2.13	11.20	11.95	89.13	0.56	150.18409	2.38638
185349	150.12357	2.22070	2.82	10.12	11.87	74.13	5.62	150.12359	2.22070
190486	150.07065	2.30516	2.94	10.45	12.07	117.49	4.17	150.07068	2.30512
193219	150.05913	2.21988	1.14	11.03	12.03	107.15	1.00	150.05923	2.21980
194663	150.15023	2.47515	1.45	12.00	13.16	1445.44	1.45	150.15023	2.47515
201627	150.05481	2.22207	0.24	8.66	8.00	0.01	0.02	150.05464	2.22203
219616	150.11419	2.22194	1.23	10.89	11.91	81.28	1.05	150.11436	2.22195
239072	150.08426	2.21848	2.86	10.40	12.47	295.12	11.75	150.08432	2.21847
239386	150.17771	2.14746	2.10	11.34	11.76	57.54	0.26	150.17773	2.14746
239718	150.17688	2.14696	2.96	10.57	12.21	162.18	4.37	150.17694	2.14697
255108	150.09940	2.40493	2.48	10.90	11.99	97.72	1.23	150.09941	2.40491
264733	150.04226	2.22635	3.97	11.61	13.36	2290.87	5.62	150.04228	2.22636
269152	150.13830	2.22500	1.78	11.50	11.73	53.70	0.17	150.13825	2.22500
270203	150.13639	2.22533	1.48	10.75	12.32	208.93	3.72	150.13630	2.22524
292194	150.02760	2.22796	1.40	11.44	12.27	186.21	0.68	150.02762	2.22797
313094	150.10535	2.31290	2.28	11.45	12.72	524.81	1.86	150.10540	2.31284
320337	150.08803	2.39510	3.42	10.51	12.49	309.03	9.55	150.08802	2.39510
333216	150.11209	2.31401	2.11	11.24	11.90	79.43	0.46	150.11215	2.31400
362264	150.16061	2.15627	2.07	10.70	12.00	100.00	2.00	150.16063	2.15627
367935	150.14822	2.15696	1.52	9.29	10.91	8.13	4.15	150.14828	2.15692
380083	150.07321	2.23324	2.33	10.56	12.15	141.25	3.89	150.07331	2.23325
404147	150.09807	2.16577	1.15	11.56	12.29	194.98	0.54	150.09809	2.16577
404453	150.09884	2.16627	1.13	11.26	12.06	114.82	0.63	150.09885	2.16623
427795	150.12057	2.41809	5.64	11.82	12.48	302.00	0.46	150.12059	2.41809

Table 6. (continued)

ALMA (A3COSMOS)								JWST (DJA)	
ID	RA [deg]	Dec [deg]	z	$\log_{10}(M_*/M_\odot)$ [dex]	$\log_{10}(L_{\text{dust}}/L_\odot)$ [dex]	SFR [$M_\odot \text{ yr}^{-1}$]	sSFR [yr^{-1}]	RA [deg]	Dec [deg]
434557	150.18781	2.16064	1.86	11.08	12.46	288.40	2.40	150.18780	2.16065
435921	150.09852	2.32084	2.70	10.37	12.21	162.18	6.92	150.09854	2.32087
443595	150.11511	2.32127	2.13	10.68	12.13	134.90	2.82	150.11511	2.32127
481073	150.16688	2.23582	1.84	10.94	11.96	91.20	1.05	150.16688	2.23582
484109	150.17185	2.24071	2.09	10.85	12.56	363.08	5.13	150.17186	2.24070
484771	150.14174	2.42569	2.82	11.01	12.32	208.93	2.04	150.14177	2.42568
486177	150.18759	2.32248	1.52	11.73	12.14	138.04	0.26	150.18760	2.32249
506425	150.10467	2.24366	1.91	11.33	12.09	123.03	0.58	150.10466	2.24367
519264	150.10520	2.32581	1.26	9.82	11.64	43.65	6.58	150.10521	2.32582
519984	150.13915	2.43197	3.07	11.63	12.58	380.19	0.89	150.13917	2.43198
527216	150.11518	2.43330	0.02	6.00	8.00	0.01	10.00	150.11515	2.43333
530894	150.09547	2.24667	2.18	10.82	12.33	213.80	3.24	150.09547	2.24668
535014	150.13895	2.43377	2.60	11.31	12.97	933.25	4.57	150.13897	2.43376
539347	150.12639	2.43285	1.27	11.11	12.16	144.54	1.12	150.12636	2.43287
539550	150.15373	2.32797	4.37	11.58	13.16	1445.44	3.80	150.15375	2.32798
572875	150.15365	2.24772	3.09	10.94	12.23	169.82	1.95	150.15365	2.24776
580664	150.10634	2.25157	2.93	11.63	13.22	1659.59	3.89	150.10632	2.25157
591583	150.12996	2.25271	2.93	11.28	12.64	436.52	2.29	150.12998	2.25268
595185	150.10934	2.25277	2.01	9.97	11.56	36.31	3.92	150.10926	2.25268
611293	150.10136	2.44270	2.24	10.45	11.73	53.70	1.91	150.10135	2.44270
614294	150.13636	2.33352	1.08	10.93	11.27	18.62	0.22	150.13630	2.33362
616447	150.15175	2.33459	1.74	11.84	12.10	125.89	0.18	150.15179	2.33460
646590	150.09458	2.33633	0.93	11.17	11.78	60.26	0.41	150.09460	2.33635
663586	150.13583	2.25792	4.45	9.63	11.64	43.65	10.30	150.13584	2.25789
665972	150.06671	2.25773	2.10	10.87	11.35	22.39	0.30	150.06670	2.25773
670959	150.07740	2.18536	2.20	11.10	12.10	125.89	1.00	150.07741	2.18536
678818	150.14722	2.33717	0.73	11.10	11.68	47.86	0.38	150.14719	2.33718
682011	150.09531	2.33895	3.13	10.61	11.92	83.18	2.04	150.09533	2.33898
685092	150.11033	2.25844	2.45	9.82	11.29	19.50	2.94	150.11039	2.25864
696095	150.10394	2.18642	2.10	11.68	12.69	489.78	1.02	150.10395	2.18642
702416	150.07933	2.34058	2.68	10.66	12.55	354.81	7.76	150.07933	2.34056
719895	150.07192	2.19020	2.80	11.51	12.40	251.19	0.78	150.07195	2.19018
754141	150.10750	2.34435	2.69	10.48	11.48	30.20	1.00	150.10754	2.34434
765691	150.08644	2.26432	1.19	9.48	12.04	109.65	36.14	150.08648	2.26430
778981	150.12575	2.26662	0.72	8.65	11.13	13.49	30.06	150.12573	2.26659
782304	150.10355	2.34608	1.03	11.01	12.00	100.00	0.98	150.10352	2.34608
812701	150.03650	2.19837	3.00	10.99	11.99	97.72	1.00	150.03651	2.19838
815643	150.03142	2.19637	3.50	10.66	13.17	1479.11	32.36	150.03142	2.19640
817083	150.17488	2.35273	2.38	10.79	12.30	199.53	3.24	150.17487	2.35274
819118	150.12487	2.26945	0.97	10.61	11.29	19.50	0.48	150.12489	2.26947
854401	150.05385	2.20323	3.17	11.42	12.72	524.81	2.00	150.05385	2.20321
865238	150.12286	2.36096	2.01	11.09	12.18	151.36	1.23	150.12290	2.36097
877714	150.14127	2.27816	2.17	10.97	11.27	18.62	0.20	150.14129	2.27819
885687	150.10877	2.20872	3.53	10.51	11.88	75.86	2.34	150.10876	2.20871

Table 6. (continued)

ALMA (A3COSMOS)								JWST (DJA)	
ID	RA [deg]	Dec [deg]	z	$\log_{10}(M_*/M_\odot)$ [dex]	$\log_{10}(L_{\text{dust}}/L_\odot)$ [dex]	SFR [$M_\odot \text{ yr}^{-1}$]	sSFR [yr^{-1}]	RA [deg]	Dec [deg]
889846	150.09596	2.36526	4.44	11.30	12.00	100.00	0.50	150.09597	2.36526
892054	150.09855	2.36538	2.56	11.61	12.75	562.34	1.38	150.09856	2.36537
893896	150.13087	2.20896	3.11	11.50	12.66	457.09	1.45	150.13088	2.20895
894877	150.10925	2.20732	1.25	11.60	12.41	257.04	0.65	150.10925	2.20734
911118	150.05975	2.28100	3.96	10.87	12.01	102.33	1.38	150.05975	2.28101
923171	150.17076	2.36861	3.36	11.15	12.43	269.15	1.91	150.17080	2.36862
931419	150.11433	2.36987	4.22	10.52	12.62	416.87	12.59	150.11432	2.36985
941026	150.16353	2.37252	2.08	11.08	12.75	562.34	4.68	150.16353	2.37248
944131	150.17157	2.28732	4.58	9.73	11.35	22.39	4.20	150.17158	2.28730
949027	150.12448	2.28950	2.86	10.52	11.37	23.44	0.71	150.12448	2.28950
954639	150.11234	2.37526	2.40	10.48	11.47	29.51	0.98	150.11236	2.37524
956001	150.14415	2.37631	3.24	10.97	11.92	83.18	0.89	150.14418	2.37632
1316680	150.10520	2.15661	1.58	10.91	12.14	138.04	1.70	150.10519	2.15664
1316752	150.13932	2.14951	1.05	11.05	12.11	128.83	1.15	150.13932	2.14953
1329539	150.05313	2.19807	1.33	11.28	12.22	165.96	0.87	150.05318	2.19808
1334731	150.14477	2.21968	1.76	10.67	11.68	47.86	1.02	150.14482	2.21971
1344523	150.09401	2.24580	1.77	10.62	12.21	162.18	3.89	150.09402	2.24586
1351031	150.18430	2.26438	1.85	10.22	11.70	50.12	3.02	150.18428	2.26436
1357333	150.19441	2.27327	0.37	8.72	10.50	3.16	6.07	150.19436	2.27331
1357956	150.14728	2.28236	1.98	10.57	12.16	144.54	3.89	150.14729	2.28233
1384974	150.14317	2.35598	1.52	10.22	12.17	147.91	8.91	150.14324	2.35602
1393572	150.06144	2.37880	2.38	10.65	12.66	457.09	10.23	150.06146	2.37871
1394965	150.06980	2.38154	2.30	9.24	11.46	28.84	16.52	150.06982	2.38152
1435854	150.11169	2.48042	1.75	11.18	12.40	251.19	1.66	150.11175	2.48042
1767929	150.07469	2.21648	1.92	11.31	12.56	363.08	1.78	150.07471	2.21648
1768691	150.11126	2.40318	2.44	10.78	12.41	257.04	4.27	150.11130	2.40318
1769008	150.10586	2.42881	2.99	11.21	12.84	691.83	4.27	150.10587	2.42881
1769044	150.10697	2.42895	0.06	7.90	8.89	0.08	0.98	150.10698	2.42894
1834187	150.10968	2.18797	2.30	11.37	12.48	302.00	1.29	150.10965	2.18794
1834514	150.09824	2.16624	1.80	11.74	12.61	407.38	0.74	150.09825	2.16625
1835014	150.12926	2.46431	3.77	11.63	13.03	1071.52	2.51	150.12929	2.46431
1835211	150.14034	2.14715	4.20	11.70	13.10	1258.93	2.51	150.14033	2.14715
1835575	150.17434	2.47825	0.54	9.17	8.39	0.03	0.02	150.17420	2.47810
1835807	150.06508	2.26363	4.60	11.09	13.31	2041.74	16.60	150.06510	2.26363
1836013	150.19625	2.17128	5.05	11.34	12.95	891.25	4.07	150.19626	2.17128
1836571	150.17427	2.42973	6.35	11.20	13.17	1479.11	9.33	150.17429	2.42973
1837147	150.10065	2.33485	5.90	11.04	13.02	1047.13	9.55	150.10064	2.33483
1845716	150.10448	2.43538	6.20	11.35	13.31	2041.74	9.12	150.10446	2.43538
1855826	150.09991	2.29711	4.00	11.39	13.22	1659.59	6.76	150.10009	2.29714
1895614	150.10982	2.25775	5.85	11.35	12.97	933.25	4.17	150.10981	2.25779

REFERENCES

- Adscheid, S., Magnelli, B., Liu, D., et al. 2024, *A&A*, 685, A1, doi: [10.1051/0004-6361/202348407](https://doi.org/10.1051/0004-6361/202348407)
- Astropy Collaboration, Robitaille, T. P., Tollerud, E. J., et al. 2013, *A&A*, 558, A33, doi: [10.1051/0004-6361/201322068](https://doi.org/10.1051/0004-6361/201322068)
- Astropy Collaboration, Price-Whelan, A. M., Sipőcz, B. M., et al. 2018, *AJ*, 156, 123, doi: [10.3847/1538-3881/aabc4f](https://doi.org/10.3847/1538-3881/aabc4f)
- Astropy Collaboration, Price-Whelan, A. M., Lim, P. L., et al. 2022, *ApJ*, 935, 167, doi: [10.3847/1538-4357/ac7c74](https://doi.org/10.3847/1538-4357/ac7c74)
- Barger, A. J., Cowie, L. L., Sanders, D. B., et al. 1998, *Nature*, 394, 248, doi: [10.1038/28338](https://doi.org/10.1038/28338)
- Baugh, C. M., Lacey, C. G., Frenk, C. S., et al. 2005, *MNRAS*, 356, 1191, doi: [10.1111/j.1365-2966.2004.08553.x](https://doi.org/10.1111/j.1365-2966.2004.08553.x)
- Benton, C. E., Nelson, E. J., Miller, T. B., et al. 2024, *ApJL*, 974, L28, doi: [10.3847/2041-8213/ad7e27](https://doi.org/10.3847/2041-8213/ad7e27)
- Bertin, E. 2013, *Astrophysics Source Code Library*, record ascl:1301.001
- Blain, A. W., Smail, I., Ivison, R. J., Kneib, J. P., & Frayer, D. T. 2002, *PhR*, 369, 111, doi: [10.1016/S0370-1573\(02\)00134-5](https://doi.org/10.1016/S0370-1573(02)00134-5)
- Bradbury, J., Frostig, R., Hawkins, P., et al. 2018, 0.3.13 <http://github.com/jax-ml/jax>
- Bradley, L., Sipőcz, B., Robitaille, T., et al. 2024, 2.0.2 Zenodo, doi: [10.5281/zenodo.13989456](https://doi.org/10.5281/zenodo.13989456)
- Brammer, G. 2023, 1.9.11 Zenodo, doi: [10.5281/zenodo.8370018](https://doi.org/10.5281/zenodo.8370018)
- Calabrò, A., Daddi, E., Fensch, J., et al. 2019, *A&A*, 632, A98, doi: [10.1051/0004-6361/201935778](https://doi.org/10.1051/0004-6361/201935778)
- Casey, C. M., Narayanan, D., & Cooray, A. 2014, *PhR*, 541, 45, doi: [10.1016/j.physrep.2014.02.009](https://doi.org/10.1016/j.physrep.2014.02.009)
- Chapman, S. C., Smail, I., Blain, A. W., & Ivison, R. J. 2004, *ApJ*, 614, 671, doi: [10.1086/423833](https://doi.org/10.1086/423833)
- Chen, C.-C., Smail, I., Swinbank, A. M., et al. 2015, *ApJ*, 799, 194, doi: [10.1088/0004-637X/799/2/194](https://doi.org/10.1088/0004-637X/799/2/194)
- Chen, C.-C., Gao, Z.-K., Hsu, Q.-N., et al. 2022, *ApJL*, 939, L7, doi: [10.3847/2041-8213/ac98c6](https://doi.org/10.3847/2041-8213/ac98c6)
- Combes, F. 2016, in *Astrophysics and Space Science Library*, Vol. 418, Galactic Bulges, ed. E. Laurikainen, R. Peletier, & D. Gadotti, 413, doi: [10.1007/978-3-319-19378-6_15](https://doi.org/10.1007/978-3-319-19378-6_15)
- Conselice, C. J. 2003, *ApJS*, 147, 1, doi: [10.1086/375001](https://doi.org/10.1086/375001)
- Conselice, C. J. 2014, *ARA&A*, 52, 291, doi: [10.1146/annurev-astro-081913-040037](https://doi.org/10.1146/annurev-astro-081913-040037)
- Conselice, C. J., Chapman, S. C., & Windhorst, R. A. 2003, *ApJL*, 596, L5, doi: [10.1086/379109](https://doi.org/10.1086/379109)
- da Cunha, E., Walter, F., Smail, I. R., et al. 2015, *ApJ*, 806, 110, doi: [10.1088/0004-637X/806/1/110](https://doi.org/10.1088/0004-637X/806/1/110)
- Davé, R., Finlator, K., Oppenheimer, B. D., et al. 2010, *MNRAS*, 404, 1355, doi: [10.1111/j.1365-2966.2010.16395.x](https://doi.org/10.1111/j.1365-2966.2010.16395.x)
- de Vaucouleurs, G., de Vaucouleurs, A., Corwin, Jr., H. G., et al. 1991, *Third Reference Catalogue of Bright Galaxies*
- Dekel, A., Birnboim, Y., Engel, G., et al. 2009, *Nature*, 457, 451, doi: [10.1038/nature07648](https://doi.org/10.1038/nature07648)
- Draper, A. R., & Ballantyne, D. R. 2012, *ApJL*, 753, L37, doi: [10.1088/2041-8205/753/2/L37](https://doi.org/10.1088/2041-8205/753/2/L37)
- Du, M., Ho, L. C., Debattista, V. P., et al. 2021, *ApJ*, 919, 135, doi: [10.3847/1538-4357/ac0e98](https://doi.org/10.3847/1538-4357/ac0e98)
- Dudzevičiūtė, U., Smail, I., Swinbank, A. M., et al. 2020, *MNRAS*, 494, 3828, doi: [10.1093/mnras/staa769](https://doi.org/10.1093/mnras/staa769)
- Elmegreen, B. G. 2009, in *Astronomical Society of the Pacific Conference Series*, Vol. 419, Galaxy Evolution: Emerging Insights and Future Challenges, ed. S. Jogee, I. Marinova, L. Hao, & G. A. Blanc, 23, doi: [10.48550/arXiv.0903.1937](https://doi.org/10.48550/arXiv.0903.1937)
- Erwin, P., Saglia, R. P., Fabricius, M., et al. 2015, *MNRAS*, 446, 4039, doi: [10.1093/mnras/stu2376](https://doi.org/10.1093/mnras/stu2376)
- Fujimoto, S., Ouchi, M., Kohno, K., et al. 2018, *ApJ*, 861, 7, doi: [10.3847/1538-4357/aac6c4](https://doi.org/10.3847/1538-4357/aac6c4)
- Fujimoto, S., Ouchi, M., Kohno, K., et al. 2024, *arXiv e-prints*, arXiv:2402.18543, doi: [10.48550/arXiv.2402.18543](https://doi.org/10.48550/arXiv.2402.18543)
- Gadotti, D. A. 2009, *MNRAS*, 393, 1531, doi: [10.1111/j.1365-2966.2008.14257.x](https://doi.org/10.1111/j.1365-2966.2008.14257.x)
- Gaia Collaboration, Brown, A. G. A., Vallenari, A., et al. 2021, *A&A*, 649, A1, doi: [10.1051/0004-6361/202039657](https://doi.org/10.1051/0004-6361/202039657)
- Gillman, S., Gullberg, B., Brammer, G., et al. 2023, *A&A*, 676, A26, doi: [10.1051/0004-6361/202346531](https://doi.org/10.1051/0004-6361/202346531)
- Gillman, S., Smail, I., Gullberg, B., et al. 2024, *A&A*, 691, A299, doi: [10.1051/0004-6361/202451006](https://doi.org/10.1051/0004-6361/202451006)
- Gonzalez, O. A., & Gadotti, D. 2016, in *Astrophysics and Space Science Library*, Vol. 418, Galactic Bulges, ed. E. Laurikainen, R. Peletier, & D. Gadotti, 199, doi: [10.1007/978-3-319-19378-6_9](https://doi.org/10.1007/978-3-319-19378-6_9)
- Grogin, N. A., Kocevski, D. D., Faber, S. M., et al. 2011, *ApJS*, 197, 35, doi: [10.1088/0067-0049/197/2/35](https://doi.org/10.1088/0067-0049/197/2/35)
- Gullberg, B., Smail, I., Swinbank, A. M., et al. 2019, *MNRAS*, 490, 4956, doi: [10.1093/mnras/stz2835](https://doi.org/10.1093/mnras/stz2835)
- Guo, Y., Jogee, S., Finkelstein, S. L., et al. 2023, *ApJL*, 945, L10, doi: [10.3847/2041-8213/acacfb](https://doi.org/10.3847/2041-8213/acacfb)
- Hauser, M. G., Arendt, R. G., Kelsall, T., et al. 1998, *ApJ*, 508, 25, doi: [10.1086/306379](https://doi.org/10.1086/306379)
- Hayward, C. C., Narayanan, D., Kereš, D., et al. 2013, *MNRAS*, 428, 2529, doi: [10.1093/mnras/sts222](https://doi.org/10.1093/mnras/sts222)

- Herrera-Endoqui, M., Díaz-García, S., Laurikainen, E., & Salo, H. 2015, *A&A*, 582, A86, doi: [10.1051/0004-6361/201526047](https://doi.org/10.1051/0004-6361/201526047)
- Hodge, J. A., Swinbank, A. M., Simpson, J. M., et al. 2016, *ApJ*, 833, 103, doi: [10.3847/1538-4357/833/1/103](https://doi.org/10.3847/1538-4357/833/1/103)
- Hodge, J. A., Smail, I., Walter, F., et al. 2019, *ApJ*, 876, 130, doi: [10.3847/1538-4357/ab1846](https://doi.org/10.3847/1538-4357/ab1846)
- Hodge, J. A., da Cunha, E., Kendrew, S., et al. 2025, *ApJ*, 978, 165, doi: [10.3847/1538-4357/ad9a52](https://doi.org/10.3847/1538-4357/ad9a52)
- Hopkins, P. F., Kereš, D., Murray, N., Quataert, E., & Hernquist, L. 2012, *MNRAS*, 427, 968, doi: [10.1111/j.1365-2966.2012.21981.x](https://doi.org/10.1111/j.1365-2966.2012.21981.x)
- Hughes, D. H., Serjeant, S., Dunlop, J., et al. 1998, *Nature*, 394, 241, doi: [10.1038/28328](https://doi.org/10.1038/28328)
- Hunter, J. D. 2007, *Computing in Science & Engineering*, 9, 90, doi: [10.1109/MCSE.2007.55](https://doi.org/10.1109/MCSE.2007.55)
- Immeli, A., Samland, M., Gerhard, O., & Westera, P. 2004, *A&A*, 413, 547, doi: [10.1051/0004-6361:20034282](https://doi.org/10.1051/0004-6361:20034282)
- Inoue, S., & Saitoh, T. R. 2012, *MNRAS*, 422, 1902, doi: [10.1111/j.1365-2966.2011.20338.x](https://doi.org/10.1111/j.1365-2966.2011.20338.x)
- Kalita, B. S., Silverman, J. D., Daddi, E., et al. 2024, *ApJ*, 960, 25, doi: [10.3847/1538-4357/acfee4](https://doi.org/10.3847/1538-4357/acfee4)
- Kartaltepe, J. S., Dickinson, M., Alexander, D. M., et al. 2012, *ApJ*, 757, 23, doi: [10.1088/0004-637X/757/1/23](https://doi.org/10.1088/0004-637X/757/1/23)
- Kokorev, V., Brammer, G., Fujimoto, S., et al. 2022, *ApJS*, 263, 38, doi: [10.3847/1538-4365/ac9909](https://doi.org/10.3847/1538-4365/ac9909)
- Kormendy, J. 2016, in *Astrophysics and Space Science Library*, Vol. 418, *Galactic Bulges*, ed. E. Laurikainen, R. Peletier, & D. Gadotti, 431, doi: [10.1007/978-3-319-19378-6_16](https://doi.org/10.1007/978-3-319-19378-6_16)
- Kormendy, J., & Bender, R. 2012, *ApJS*, 198, 2, doi: [10.1088/0067-0049/198/1/2](https://doi.org/10.1088/0067-0049/198/1/2)
- Kormendy, J., & Kennicutt, Jr., R. C. 2004, *ARA&A*, 42, 603, doi: [10.1146/annurev.astro.42.053102.134024](https://doi.org/10.1146/annurev.astro.42.053102.134024)
- Laurikainen, E., Salo, H., & Buta, R. 2005, *MNRAS*, 362, 1319, doi: [10.1111/j.1365-2966.2005.09404.x](https://doi.org/10.1111/j.1365-2966.2005.09404.x)
- Le Bail, A., Daddi, E., Elbaz, D., et al. 2024, *A&A*, 688, A53, doi: [10.1051/0004-6361/202347465](https://doi.org/10.1051/0004-6361/202347465)
- Le Conte, Z. A., Gadotti, D. A., Ferreira, L., et al. 2024, *MNRAS*, 530, 1984, doi: [10.1093/mnras/stae921](https://doi.org/10.1093/mnras/stae921)
- Leauthaud, A., Massey, R., Kneib, J.-P., et al. 2007, *ApJS*, 172, 219, doi: [10.1086/516598](https://doi.org/10.1086/516598)
- Liang, X., Yu, S.-Y., Fang, T., & Ho, L. C. 2024, *A&A*, 688, A158, doi: [10.1051/0004-6361/202348539](https://doi.org/10.1051/0004-6361/202348539)
- Liu, D., Lang, P., Magnelli, B., et al. 2019, *ApJS*, 244, 40, doi: [10.3847/1538-4365/ab42da](https://doi.org/10.3847/1538-4365/ab42da)
- Lonsdale, C. J., Farrah, D., & Smith, H. E. 2006, in *Astrophysics Update 2*, ed. J. W. Mason, 285, doi: [10.1007/3-540-30313-8_9](https://doi.org/10.1007/3-540-30313-8_9)
- Lotz, J. M., Primack, J., & Madau, P. 2004, *AJ*, 128, 163, doi: [10.1086/421849](https://doi.org/10.1086/421849)
- Lotz, J. M., Davis, M., Faber, S. M., et al. 2008, *ApJ*, 672, 177, doi: [10.1086/523659](https://doi.org/10.1086/523659)
- Lu, S., Du, M., & Debattista, V. P. 2025, *A&A*, 697, A236, doi: [10.1051/0004-6361/202453143](https://doi.org/10.1051/0004-6361/202453143)
- Ma, H.-C., Du, M., Ho, L. C., Sheng, M.-J., & Liao, S. 2024, *A&A*, 689, A293, doi: [10.1051/0004-6361/202450397](https://doi.org/10.1051/0004-6361/202450397)
- Marinova, I., & Jogee, S. 2007, *ApJ*, 659, 1176, doi: [10.1086/512355](https://doi.org/10.1086/512355)
- McKay, S. J., Barger, A. J., Cowie, L. L., & Nicandro Rosenthal, M. J. 2025, *arXiv e-prints*, arXiv:2503.00102, doi: [10.48550/arXiv.2503.00102](https://doi.org/10.48550/arXiv.2503.00102)
- McKinney, J., Casey, C. M., Long, A. S., et al. 2025, *ApJ*, 979, 229, doi: [10.3847/1538-4357/ada357](https://doi.org/10.3847/1538-4357/ada357)
- Menéndez-Delmestre, K., Sheth, K., Schinnerer, E., Jarrett, T. H., & Scoville, N. Z. 2007, *ApJ*, 657, 790, doi: [10.1086/511025](https://doi.org/10.1086/511025)
- Meng, X., & Gnedin, O. Y. 2020, *MNRAS*, 494, 1263, doi: [10.1093/mnras/staa776](https://doi.org/10.1093/mnras/staa776)
- Nair, P. B., & Abraham, R. G. 2010, *ApJS*, 186, 427, doi: [10.1088/0067-0049/186/2/427](https://doi.org/10.1088/0067-0049/186/2/427)
- Narayanan, D., Turk, M., Feldmann, R., et al. 2015, *Nature*, 525, 496, doi: [10.1038/nature15383](https://doi.org/10.1038/nature15383)
- Nevin, B., Comerford, J., Blecha, L., & Greene, J. 2019, in *American Astronomical Society Meeting Abstracts*, Vol. 233, *American Astronomical Society Meeting Abstracts #233*, 128.05
- Noguchi, M. 2000, *MNRAS*, 312, 194, doi: [10.1046/j.1365-8711.2000.03130.x](https://doi.org/10.1046/j.1365-8711.2000.03130.x)
- Oklopčić, A., Hopkins, P. F., Feldmann, R., et al. 2017, *MNRAS*, 465, 952, doi: [10.1093/mnras/stw2754](https://doi.org/10.1093/mnras/stw2754)
- Pasha, I., & Miller, T. B. 2023, *The Journal of Open Source Software*, 8, 5703, doi: [10.21105/joss.05703](https://doi.org/10.21105/joss.05703)
- Peng, C. Y., Ho, L. C., Impey, C. D., & Rix, H.-W. 2010, *AJ*, 139, 2097, doi: [10.1088/0004-6256/139/6/2097](https://doi.org/10.1088/0004-6256/139/6/2097)
- Pereira-Santaella, M., Colina, L., García-Burillo, S., et al. 2021, *A&A*, 651, A42, doi: [10.1051/0004-6361/202140955](https://doi.org/10.1051/0004-6361/202140955)
- Perna, M., Arribas, S., Pereira Santaella, M., et al. 2021, *A&A*, 646, A101, doi: [10.1051/0004-6361/202039702](https://doi.org/10.1051/0004-6361/202039702)
- Perna, M., Arribas, S., Colina, L., et al. 2022, *A&A*, 662, A94, doi: [10.1051/0004-6361/202142659](https://doi.org/10.1051/0004-6361/202142659)
- Phan, D., Pradhan, N., & Jankowiak, M. 2019, *arXiv e-prints*, arXiv:1912.11554, doi: [10.48550/arXiv.1912.11554](https://doi.org/10.48550/arXiv.1912.11554)
- Puget, J. L., Abergel, A., Bernard, J. P., et al. 1996, *A&A*, 308, L5
- Ren, J., Liu, F. S., Li, N., et al. 2025a, *arXiv e-prints*, arXiv:2502.15569, doi: [10.48550/arXiv.2502.15569](https://doi.org/10.48550/arXiv.2502.15569)

- Ren, J., Liu, F. S., Li, N., et al. 2025b, *ApJ*, 982, 200, doi: [10.3847/1538-4357/adb961](https://doi.org/10.3847/1538-4357/adb961)
- Riechers, D. A., Capak, P. L., Carilli, C. L., et al. 2010, *ApJL*, 720, L131, doi: [10.1088/2041-8205/720/2/L131](https://doi.org/10.1088/2041-8205/720/2/L131)
- Rodriguez-Gomez, V., Snyder, G. F., Lotz, J. M., et al. 2019, *MNRAS*, 483, 4140, doi: [10.1093/mnras/sty3345](https://doi.org/10.1093/mnras/sty3345)
- Saha, K., Gerhard, O., & Martinez-Valpuesta, I. 2016, *A&A*, 588, A42, doi: [10.1051/0004-6361/201527566](https://doi.org/10.1051/0004-6361/201527566)
- Saha, K., Martinez-Valpuesta, I., & Gerhard, O. 2012, *MNRAS*, 421, 333, doi: [10.1111/j.1365-2966.2011.20307.x](https://doi.org/10.1111/j.1365-2966.2011.20307.x)
- Salo, H., Laurikainen, E., Laine, J., et al. 2015, *ApJS*, 219, 4, doi: [10.1088/0067-0049/219/1/4](https://doi.org/10.1088/0067-0049/219/1/4)
- Sanders, D. B., & Mirabel, I. F. 1996, *ARA&A*, 34, 749, doi: [10.1146/annurev.astro.34.1.749](https://doi.org/10.1146/annurev.astro.34.1.749)
- Sheth, K., Elmegreen, D. M., Elmegreen, B. G., et al. 2008, *ApJ*, 675, 1141, doi: [10.1086/524980](https://doi.org/10.1086/524980)
- Simpson, J. M., Swinbank, A. M., Smail, I., et al. 2014, *ApJ*, 788, 125, doi: [10.1088/0004-637X/788/2/125](https://doi.org/10.1088/0004-637X/788/2/125)
- Smail, I., Chapman, S. C., Blain, A. W., & Ivison, R. J. 2004, *ApJ*, 616, 71, doi: [10.1086/424896](https://doi.org/10.1086/424896)
- Smail, I., Ivison, R. J., & Blain, A. W. 1997, *ApJL*, 490, L5, doi: [10.1086/311017](https://doi.org/10.1086/311017)
- Smail, I., Dudzevičiūtė, U., Stach, S. M., et al. 2021, *MNRAS*, 502, 3426, doi: [10.1093/mnras/stab283](https://doi.org/10.1093/mnras/stab283)
- Swinbank, A. M., Smail, I., Chapman, S. C., et al. 2010, *MNRAS*, 405, 234, doi: [10.1111/j.1365-2966.2010.16485.x](https://doi.org/10.1111/j.1365-2966.2010.16485.x)
- Tacconi, L. J., Neri, R., Chapman, S. C., et al. 2006, *ApJ*, 640, 228, doi: [10.1086/499933](https://doi.org/10.1086/499933)
- Tan, Q.-H., Daddi, E., Magnelli, B., et al. 2024, *Nature*, 636, 69, doi: [10.1038/s41586-024-08201-6](https://doi.org/10.1038/s41586-024-08201-6)
- Taylor, M. 2017, arXiv e-prints, arXiv:1711.01885, doi: [10.48550/arXiv.1711.01885](https://doi.org/10.48550/arXiv.1711.01885)
- Trujillo, I., Erwin, P., Asensio Ramos, A., & Graham, A. W. 2004, *AJ*, 127, 1917, doi: [10.1086/382712](https://doi.org/10.1086/382712)
- Valentino, F., Brammer, G., Gould, K. M. L., et al. 2023, *ApJ*, 947, 20, doi: [10.3847/1538-4357/acbefa](https://doi.org/10.3847/1538-4357/acbefa)
- Yu, S.-Y., & Ho, L. C. 2020, *ApJ*, 900, 150, doi: [10.3847/1538-4357/abac5b](https://doi.org/10.3847/1538-4357/abac5b)
- Zhang, Y., Setton, D. J., Price, S. H., et al. 2024, *ApJ*, 976, 36, doi: [10.3847/1538-4357/ad7c45](https://doi.org/10.3847/1538-4357/ad7c45)